Tailoring Light with Photonic Crystal Slabs: From Directional Emission to Topological Half Charges

by

Hengyun Zhou

Submitted to the Department of Physics
in partial fulfillment of the requirements for the degree of

Bachelor of Science in Physics

at the

MASSACHUSETTS INSTITUTE OF TECHNOLOGY

June 2016

Author ..... Signature redacted .....
Department of Physics
May 6, 2016

Certified by ..... Signature redacted
Marin Soljačić
Professor of Physics and MacArthur Fellow
Thesis Supervisor

Accepted by ..... Signature redacted
Nergis Mavalvala
Senior Thesis Coordinator, Department of Physics

Tailoring Light with Photonic Crystal Slabs: From Directional Emission to Topological Half Charges

by

Hengyun Zhou

Submitted to the Department of Physics
on May 6, 2016, in partial fulfillment of the
requirements for the degree of
Bachelor of Science in Physics

Abstract

Photonic crystal slabs are a versatile and important platform for molding the flow of light. In this thesis, we consider ways to control the emission of light from photonic crystal slab structures, specifically focusing on directional, asymmetric emission, and on emitting light with interesting topological features.

First, we develop a general coupled-mode theory formalism to derive bounds on the asymmetric decay rates to top and bottom of a photonic crystal slab, for a resonance with arbitrary in-plane wavevector. We then employ this formalism to inversion-symmetric structures, and show through numerical simulations that asymmetries of top-down decay rates exceeding 10^4 can be achieved by tuning the resonance frequency to coincide with the perfectly transmitting Fabry-Perot frequency. The emission direction can also be rapidly switched from top to bottom by tuning the wavevector or frequency.

We then consider the generation of Mobius strips of light polarization, i.e. vector beams with half-integer polarization winding, from photonic crystal slabs. We show that a quadratic degeneracy formed by symmetry considerations can be split into a pair of Dirac points, which can be further split into four exceptional points. Through calculations of an analytical two-band model and numerical simulations of two-dimensional photonic crystals and photonic crystal slabs, we demonstrate the existence of isofrequency contours encircling two exceptional points, and show the half-integer polarization winding along these isofrequency contours. We further propose a realistic photonic crystal slab structure and experimental setup to verify the existence of such Mobius strips of light polarization.

Thesis Supervisor: Marin Soljačić
Title: Professor of Physics and MacArthur Fellow

Acknowledgments

First and foremost, I would like to thank my thesis supervisor Prof. Marin Soljačić for giving me the opportunity to work in his group and for all his help and supervision on these projects. I would also like to thank Dr. Bo Zhen for directly supervising these projects and suggesting which directions to pursue with them. I have benefited immensely from frequent discussions (and occasional free lunches) with him, and have learned a lot about optics and photonics from him. This thesis would not have been possible without them.

In the course of this research, I have also greatly enjoyed my interactions with Prof. John D. Joannopoulos and Prof. Steven G. Johnson, as well as members of the Soljačić, JDJ and SGJ groups. In particular, many thanks to Nicholas Rivera and Yichen Shen for explaining their work to me and getting me interested way before I joined the group, as well as Francisco Machado, Emma Regan, Scott Skirlo, Yi Yang, Xiao Lin, Josue Lopez, Adi Pick, Dr. Ling Lu, Dr. Ognjen Ilic, Dr. Ido Kaminer and Dr. Thomas Christensen for many interesting and inspiring discussions during my time here.

It has been a great pleasure to work and study in the physics and mathematics departments at MIT. Even the most incomplete of lists of thanks here would have to include Casey and Francisco for enduring the best and worst of junior lab with me, Kamphol, Hongwan and Andrew for insights on QFT at 3 am, Nick, Yijun, Kuan-Yu, Diptarka, Tomohiro, Haoyu and many others for countless physics adventures together, and Yijun, Yibo, Yuzhou and others for all the fun we had together beginning from our first days at MIT. I would also like to thank the professors who have taught me interesting topics, as well as Prof. Vladan Vuletić, Prof. Nuh Gedik, Boris Braverman, Akio Kawasaki, Dr. Byron Freelon, Dr. Timm Rohwer and Prof. Oskar Painter and Greg MacCabe of Caltech, Prof. Yayu Wang of Tsinghua University, Prof. Heng Fan of CAS and Prof. Liangzhu Mu of Peking University for giving me the opportunity to work in their group and supervising me on research projects over the course of my undergraduate years.

Last but not least, I would like to thank my extended family, especially my parents, grandparents and grandaunt, for all the support and encouragement over the years. My deepest gratitude goes to my parents, among the uncountable other things, for stimulating my interest in science and teaching me how to be a nice person. One of them brought *Scientific American*, *New Scientist* and *Physics Today* home, and taught me how to explore broadly and learn from others; the other, through wacky theories of nearly everything in the world, taught me the importance of independent and critical thinking. To them, I present Fig. 3-6(b). This thesis is dedicated to them.

Contents

List of Figures

List of Tables

Chapter 1

Introduction

In the past few decades, there has been substantial progress in our ability to control and manipulate the flow of light. Technological progress in fabrication methods has allowed nanoscale structures to be produced with all kinds of interesting properties induced by wavelength-scale patterning of the structure, while computational methods and theoretical tools have facilitated rapid design of such structures for different physics and applications.

In this context, photonic crystals [1] have emerged as an important concept for the control of light. These are periodic dielectric structures in which the periodicity gives rise to a band structure resembling that of a conventional crystal. The dispersion relations coming from such a band structure can have interesting properties, such as photonic band gaps where light propagation is prohibited [2], or zero group velocity where slow light effects and strong interactions can be observed [3].

In many practical systems, one must also consider how the photonic structures couple to the external environment, as this may have a critical effect on the achievable quality factors and out-coupling efficiencies. The external environment generally consists of air or some substrate, in which the far-field electromagnetic eigenmodes can be taken to be propagating plane waves. In general, a resonance of the structure with the same frequency and wave vector can couple to the continuum of these external states, thus becoming leaky.

As the far field leakage radiation often corresponds to our probes of the system, it is

desirable to design and engineer the emission in the far field to have certain properties. In particular, if we wish to efficiently couple light out of the system, highly directional emission into the far field is desired, and emission towards the substrate should be minimized. On the other hand, tailoring the emitted light to have nontrivial topology of polarization directions is also of great importance for various applications [4].

In this thesis, we consider ways to control the directionality and topology of light emitted from a photonic crystal slab.

In chapter 2, we focus on directionality and asymmetry to top and bottom directions. By introducing a novel temporal coupled-mode theory formalism at finite wavevector, we derive fundamental bounds to the amount of asymmetric emission to top and bottom that can be achieved for arbitrary suspended photonic crystal slabs that satisfy some basic assumptions. The resulting reflection and transmission spectrum is also derived under this formalism. Focusing on the specific case of an inversion-symmetric structure, we show through numerical simulations that the bounds we derived are indeed satisfied, and we show examples of highly asymmetric emission when the resonance frequency is tuned to coincide with the perfectly transmitting frequency of the Fabry-Perot background. The feasibility of our proposal and some practical limitations are then discussed.

In chapter 3, we shift our attention to engineering interesting topological features in the emitted light. In particular, we demonstrate the feasibility of generating Mobius strips of polarization from a standard photonic crystal, without the need of any carefully-engineered spatial defects as in conventional q-plates. We start from an analytical two-band model, showing how symmetry breaking and addition of loss can split a symmetry-protected quadratic degeneracy into a pair of Dirac points, and further into four exceptional points. Typical frequency contours and decay rates are shown, corresponding to realistic band structures in 2D photonic crystals, and more results are shown in the appendix. We then perform numerical simulations of a 2D photonic crystal that is infinite in the third dimension to determine the band structure and polarization winding, clearly demonstrating the existence of closed isofrequency contours with half-integer polarization winding arising from the Berry phase around

Dirac points. Simulations of photonic crystal slabs with realistic parameters are performed, consistent with the analytical model and 2D simulations, and the existence of exceptional points within the isofrequency contours is shown. Finally, we propose an experimental scheme to measure the Mobius strip polarization and verify the topological winding of polarization. Our results connect the fields of topological photonics and singular optics, and illustrate that concepts such as Berry phases can have an important effect on polarization configurations.

Finally, in chapter 4, we summarize our results and offer an outlook towards other interesting possibilities that our work here opens up.

Chapter 2

Highly Asymmetric Radiation from Photonic Crystal Slabs

Due to their ease of fabrication and integration as well as their large area and high quality factor of resonances [5, 6], photonic crystal slabs [7] have been widely used in many applications. For more efficient extraction of light, it is often desirable to achieve highly asymmetric out-of-plane coupling of light to photonic crystal slabs, in which light predominantly radiates to only one side of the slab. This would eliminate the need of a back-reflection mirror in high-power photonic crystal surface emitting lasers [8], and could lead to increased efficiency in grating couplers and light detection and ranging (LIDAR) devices. Previous designs of grating couplers have achieved a top-down emission ratio of up to 50:1 [9, 10, 11], but these designs typically either make use of a reflector in the substrate or involve multiple layers and grooves [12], which not only complicate fabrication but could also be difficult to scale to larger areas if desired; asymmetric out-of-plane emission from photonic crystal defect cavities of 80% has also been demonstrated [13], but all these works were guided primarily by numerical optimization. It is thus desirable to gain an understanding of the fundamental bounds on asymmetric emission through more theoretical considerations. Previous work [14] has examined bounds of asymmetric emission for a restricted class of photonic crystal slabs with C_2^z symmetry (180° rotation around the out-of-plane axis), yielding very limited asymmetric ratios for realistic material choices, but a

general bound for arbitrary structures has not been derived.

In this chapter, we develop a general temporal coupled-mode theory (TCMT) formalism [15, 16] to derive bounds on the asymmetric decay rates of a resonance to top and bottom for arbitrary in-plane momentum ($\vec{k}$-vector). Our formalism is novel in that the time-reversal operation flips the $\vec{k}_{\|}$ of the resonance, thereby changing the form of the equations. We then employ this formalism to inversion-symmetric (P-symmetric) structures, and show through numerical simulations that asymmetries of top-down decay rates exceeding 10^4 can be achieved by tuning the resonance frequency to coincide with the perfectly transmitting Fabry-Perot frequency. The emission direction can also be rapidly switched from top to bottom by tuning the $\vec{k}$-vector or frequency. These results may provide important design principles for photonic crystal surface emitting lasers (PCSELs), grating couplers, and many other applications that could benefit from directional emission and rapid tuning. In addition, we also derive analytical expressions for the transmission spectrum and discuss features such as full transmission or reflection.

2.1 Temporal Coupled-Mode Theory Formalism with Finite Wavevector

In this section, we consider arbitrary photonic crystal slab structures embedded in a uniform medium (identical substrate and superstrate). We assume they are weakly coupled to the external environment and satisfy linearity, energy conservation and time-reversal symmetry. We employ a general temporal coupled-mode theory (TCMT) formalism to derive bounds relating the decay rates in different directions. As opposed to previous work that implicitly assumed normal incidence of light or 180 degree rotational symmetry around the out-of-plane axis (C_2^z symmetry) of the photonic crystal structure [14], we consider arbitrary incident angles and arbitrary shapes of the periodic structure.

For a plane wave with in-plane $\vec{k}$-vector $\vec{k}_{\|} = (k_x, k_y)$ incident from the top (port

1, see Fig. 2-1), by conservation of in-plane momentum due to the periodicity of the structure (neglecting higher-order diffraction), this plane wave will only couple to resonances and outgoing waves with the same $\vec{k}_{\|}$. We shall consider the typical case where there is a single resonance of interest, with the transmission spectrum consisting of a Fabry-Perot background and sharp resonant features, as in Fig. 2-2 (This frequency spectrum was calculated using the rigorous coupled-wave analysis (RCWA) method [17] with a freely available software package [18]). Assuming that there is only one resonant mode in the frequency range of interest, and writing down a similar expression for the time-reversal conjugate incoming and outgoing waves and resonances, we have the TCMT equations

$$\frac{da_1}{dt} = \left(j\omega_1 - \frac{1}{T_1}\right) a_1 + \begin{pmatrix} \kappa_1 & 0 & \kappa_3 & 0 \end{pmatrix} \begin{pmatrix} s_{1+} \\ s_{2+} \\ s_{3+} \\ s_{4+} \end{pmatrix}, \tag{2.1}$$

$$\frac{da_2}{dt} = \left(j\omega_2 - \frac{1}{T_2}\right) a_2 + \begin{pmatrix} 0 & \kappa_2 & 0 & \kappa_4 \end{pmatrix} \begin{pmatrix} s_{1+} \\ s_{2+} \\ s_{3+} \\ s_{4+} \end{pmatrix}, \tag{2.2}$$

$$\begin{pmatrix} s_{1-} \\ s_{2-} \\ s_{3-} \\ s_{4-} \end{pmatrix} = C \begin{pmatrix} s_{1+} \\ s_{2+} \\ s_{3+} \\ s_{4+} \end{pmatrix} + \begin{pmatrix} 0 & d_1 \\ d_2 & 0 \\ 0 & d_3 \\ d_4 & 0 \end{pmatrix} \begin{pmatrix} a_1 \\ a_2 \end{pmatrix}, \tag{2.3}$$

where a_i are the resonance amplitudes, ω_i and T_i are the resonance frequencies and $1/e$-decay times, s_{j+} and s_{j-} are the incoming and outgoing waves (in the following, we use $|s_+\rangle$ to denote the vector formed by these components), κ_i are the coupling rates from the incoming waves to the resonance, d_i are the coupling rates from the resonance to the outgoing waves, and C is the direct process Fabry-Perot scattering matrix. An important difference between this formalism and previous TCMT for-

malisms [15] is that we have included only terms that have the same $\vec{k}_{\|}$, as required by momentum conservation, and the time-reversal operation maps one resonance into the other resonance, instead of itself.

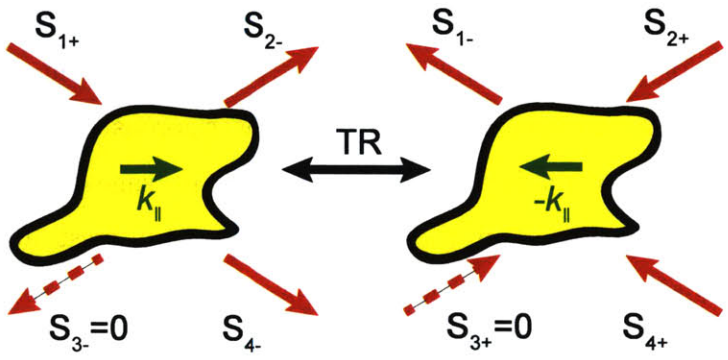

Figure 2-1: Schematic of our temporal coupled-mode theory (TCMT) setup with four ports and two resonances related by time reversal operations. This general setup is true for structures with arbitrary shapes and incident angles.

We have assumed that the system satisfies energy conservation and time reversal symmetry. In particular, this implies that the direct scattering pathway matrix C must be unitary (energy conservation) and symmetric (reciprocity) [16]. Assuming identical substrate and superstrate, and that the Fabry-Perot contribution is not affected by the details of the patterning that give rise to sharp resonances, C takes the form

$$C = e^{j\phi} \begin{pmatrix} 0 & r & 0 & jt \\ r & 0 & jt & 0 \\ 0 & jt & 0 & r \\ jt & 0 & r & 0 \end{pmatrix}, \tag{2.4}$$

where t and r are real numbers satisfying $r^2 + t^2 = 1$ that characterize the Fabry-Perot background amplitude transmission and reflection coefficients, ϕ depends on the choice of reference plane position for the phases of the waves, and the imaginary unit[1] j comes from our phase convention.

[1]In this chapter, we use the notation of electrical engineers and denote $\sqrt{-1}$ as j, while in the

Consider the process where there is no incoming wave $|s_+\rangle = 0$ and there is only one resonance that is excited $a_1(0) = a_{10}$, $a_2(0) = 0$. By energy conservation, we have

$$\frac{d(a_1^* a_1)}{dt} = -\frac{2}{T_1} a_1^* a_1 = -\langle s_-|s_-\rangle = -a_1^* a_1(|d_2|^2 + |d_4|^2), \tag{2.5}$$

which reduces to (making use of a similar equation for the second resonance)

$$|d_2|^2 + |d_4|^2 = \frac{2}{T_1}, |d_1|^2 + |d_3|^2 = \frac{2}{T_2}. \tag{2.6}$$

Now consider the time-reversed process where we send in an exponentially growing wave with initial amplitude $|s_-\rangle^*$ and frequency $\omega_1 - \frac{j}{T_1}$. Since the time-reverse of resonance 1 is resonance 2, we expect an exponentially growing amplitude in resonance 2 with no amplitude in resonance 1 or the output ports.

The amplitude equation of resonance 2 reads

$$[j(\omega_1 - \frac{j}{T_1}) - j\omega_2 + \frac{1}{T_2}]a_2 = \kappa_2 s'_{2+} + \kappa_4 s'_{4+} = \kappa_2 s^*_{2-} + \kappa_4 s^*_{4-} = \kappa_2 d_2^* a_1^* + \kappa_4 d_4^* a_1^*. \tag{2.7}$$

Due to time-reversal symmetry, $\omega_1 = \omega_2$ and $T_1 = T_2 = \tau$, so using Eq. (2.6) and Eq. (2.7), we have

$$\kappa_2 d_2^* + \kappa_4 d_4^* = d_2 d_2^* + d_4 d_4^*. \tag{2.8}$$

Following an independent port diagonalization argument presented in Ref. [15], in which the resonances and ports are rewrite in normal modes to give independent equations, Eq. (2.8) implies that $\kappa_2 = d_2$ and $\kappa_4 = d_4$. Similarly, we shall find that $\kappa_1 = d_1$ and $\kappa_3 = d_3$.

The condition that no amplitude is observed in resonance 1 in the time-reversed

next chapter, we use the notation of physicists and denote $\sqrt{-1}$ as i. This is to be consistent with the primary literature related to these works, and which is better is up for the reader to judge.

process implies that

$$e^{j\phi}\begin{pmatrix} 0 & r & 0 & jt \\ r & 0 & jt & 0 \\ 0 & jt & 0 & r \\ jt & 0 & r & 0 \end{pmatrix}\begin{pmatrix} 0 \\ d_2^* a_1^* \\ 0 \\ d_4^* a_1^* \end{pmatrix} + \begin{pmatrix} 0 & d_1 \\ d_2 & 0 \\ 0 & d_3 \\ d_4 & 0 \end{pmatrix}\begin{pmatrix} 0 \\ a_1^* \end{pmatrix} = 0, \tag{2.9}$$

which expands to two independent equations (the other two equations are linear superpositions of these and their complex conjugates)

$$e^{j\phi}(rd_2^* + jtd_4^*) + d_1 = 0, \tag{2.10}$$

$$e^{j\phi}(jtd_2^* + rd_4^*) + d_3 = 0. \tag{2.11}$$

Eqs. (2.6, 2.10, 2.11) impose constraints on the values and phases of the couplings, and hence constrain the transmission spectrum and bounds on the asymmetric coupling ratios.

2.2 Reflection and Transmission Spectra

From the preceding equations, we can derive an expression for the transmission spectrum [14, 16] that only depends on the frequencies and decay rates of the resonances and the transmission and reflection coefficients of the direct Fabry-Perot pathway.

As derived above from the time-reversal symmetry condition, we have the constraints Eqs. (2.10, 2.11). The angle ϕ there corresponds to a choice of the reference plane location. We may fix this phase to 0 by appropriately choosing our reference plane location.

Generally, the full scattering matrix including the direct pathway and resonance pathway is given by [15]

$$S = C + \frac{|d\rangle\langle\kappa|^*}{j(\omega - \omega_0) + \frac{1}{\tau}}, \tag{2.12}$$

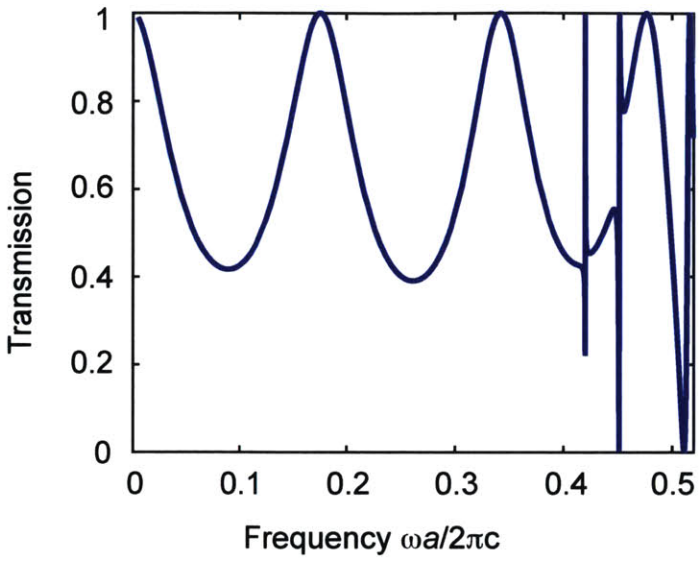

Figure 2-2: Typical transmission spectrum from an inversion-symmetric structure, exhibiting resonance peaks on top of a Fabry-Perot background.

here the τ is labeling the total decay rate to all channels of either of the resonances. We have used the fact that $\omega_1 = \omega_2$ and $T_1 = T_2$ by time-reversal symmetry of the system.

The power reflection coefficient corresponds to the amplitude squared of the (1,2) element of the scattering matrix. Using the fact that $\kappa_i = d_i$, we have

$$R = |S_{12}|^2 = \left| e^{j\phi} r + \frac{d_1 d_2}{j(\omega - \omega_0) + \frac{1}{\tau}} \right|^2 . \tag{2.13}$$

This expression can be simplified to a form that explicitly exhibits features such as full transmission and/or full reflection, and eliminates explicit dependence on the phases of the coupling rates. This is accomplished by taking the norm of the time-reversal relations.

First, let us write the decay rates to different ports as $d_i = \sqrt{\frac{1}{\tau_i}} e^{j\theta_i}$. We wish to find $\theta_1 + \theta_2$, which will allow us to evaluate the preceding expression. Eq. (2.10,2.11)

can be written as

$$r\sqrt{\frac{2}{\tau_2}}e^{-j\theta_2} + jt\sqrt{\frac{2}{\tau_4}}e^{-j\theta_4} + \sqrt{\frac{2}{\tau_1}}e^{j\theta_1} = 0, \tag{2.14}$$

$$jt\sqrt{\frac{2}{\tau_2}}e^{-j\theta_2} + r\sqrt{\frac{2}{\tau_4}}e^{-j\theta_4} + \sqrt{\frac{2}{\tau_3}}e^{j\theta_3} = 0. \tag{2.15}$$

These equations can be used to prove that $\tau_1 + \tau_3 = \tau_2 + \tau_4$, where τ_i corresponds to decays into channel i. This, combined with Eq. (2.6), implies self-consistently that the two resonances have the same decay rate.

Defining $\alpha = \theta_1 + \theta_2$, $\beta = \theta_1 + \theta_4$, the preceding equation reads

$$\sqrt{\frac{2}{\tau_1}} = -r\sqrt{\frac{2}{\tau_2}}e^{-j\alpha} - jt\sqrt{\frac{2}{\tau_4}}e^{-j\beta}, \tag{2.16}$$

$$\sqrt{\frac{2}{\tau_3}}e^{j\theta_3 - j\theta_1} = -jt\sqrt{\frac{2}{\tau_2}}e^{-j\alpha} - r\sqrt{\frac{2}{\tau_4}}e^{-j\beta}. \tag{2.17}$$

Taking the norm squared of both sides, we obtain

$$\frac{2}{\tau_1} = \frac{2r^2}{\tau_2} + \frac{2t^2}{\tau_4} - \frac{4rt}{\sqrt{\tau_2\tau_4}}\sin(\alpha - \beta) \tag{2.18}$$

$$\frac{2}{\tau_3} = \frac{2r^2}{\tau_4} + \frac{2t^2}{\tau_2} + \frac{4rt}{\sqrt{\tau_2\tau_4}}\sin(\alpha - \beta) \tag{2.19}$$

Adding these two equations, we find

$$\frac{1}{T_2} = \frac{1}{\tau_1} + \frac{1}{\tau_3} = \frac{1}{\tau_2} + \frac{1}{\tau_4} = \frac{1}{T_1}, \tag{2.20}$$

as desired.

Now we solve for the transmission spectrum by solving α. Moving the term containing α over to the left hand side in Eq. (2.16) and taking the norm squared gives

$$\frac{2t^2}{\tau_4} = \frac{2r^2}{\tau_2} + \frac{2}{\tau_1} + \frac{4r\cos\alpha}{\sqrt{\tau_1\tau_2}}. \tag{2.21}$$

To simplify the preceding expression, we write

$$\frac{1}{\tau} = \frac{1}{\tau_1} + \frac{1}{\tau_3} = \frac{1}{\tau_2} + \frac{1}{\tau_4}, \quad \frac{1}{\sigma} = \frac{1}{\tau_1} - \frac{1}{\tau_4}, \tag{2.22}$$

and thus

$$\cos\alpha = \frac{\sqrt{\tau_1\tau_2}}{2r}\left(-\frac{r^2}{\tau} - \frac{1}{\sigma}\right) \tag{2.23}$$

$$\sin\alpha = \pm\sqrt{1 - \frac{\tau_1\tau_2}{4r^2}\left(\frac{r^2}{\tau} + \frac{1}{\sigma}\right)^2} = \pm\frac{\sqrt{\tau_1\tau_2}}{2}\sqrt{\frac{4}{\tau_1\tau_2} - \frac{r^2}{\tau^2} - \frac{2}{\tau\sigma} - \frac{1}{\sigma^2 r^2}} \tag{2.24}$$

The reflectance given by Eq. (2.13) can be written as

$$\begin{aligned} R &= \frac{|rj(\omega-\omega_0) + \frac{r}{\tau} + \frac{2}{\sqrt{\tau_1\tau_2}}(\cos\alpha + j\sin\alpha)|^2}{(\omega-\omega_0)^2 + \frac{1}{\tau^2}} \\ &= \frac{r^2(\omega-\omega_0)^2 + \frac{r^2}{\tau^2} + \frac{4}{\tau_1\tau_2} + \frac{4r\cos\alpha}{\tau\sqrt{\tau_1\tau_2}} + \frac{4r(\omega-\omega_0)\sin\alpha}{\sqrt{\tau_1\tau_2}}}{(\omega-\omega_0)^2 + \frac{1}{\tau^2}} \\ &= \frac{\left[r(\omega-\omega_0) \pm \sqrt{\frac{4}{\tau_1\tau_2} - \frac{r^2}{\tau^2} - \frac{2}{\tau\sigma} - \frac{1}{\sigma^2 r^2}}\right]^2 + (\frac{1}{\sigma r})^2}{(\omega-\omega_0)^2 + \frac{1}{\tau^2}}, \end{aligned} \tag{2.25}$$

where the last line can be directly verified by expanding all terms using Eqs. (2.22-2.24) given above. This expression is similar to Eq. (12) of Ref. [14], except that here because τ_1 and τ_2 are not necessarily identical, the form of the expression within the square root is different.

The expression in the square root in Eq. (2.25) is given by

$$\begin{aligned} \frac{4}{\tau_1\tau_2} - \frac{2}{\tau\sigma} - \frac{r^2}{\tau^2} - \frac{1}{\sigma^2 r^2} &= \frac{4}{\tau_1\tau_2} - 2\left(\frac{1}{\tau_1} - \frac{1}{\tau_4}\right)\left(\frac{1}{\tau_2} + \frac{1}{\tau_4}\right) - \frac{r^2}{\tau^2} - \frac{1}{\sigma^2 r^2} \\ &= \frac{2}{\tau_1\tau_2} + \frac{2}{\tau_4^2} + \frac{2}{\tau_4}\left(\frac{1}{\tau_2} - \frac{1}{\tau_1}\right) - \frac{r^2}{\tau^2} - \frac{1}{\sigma^2 r^2}, \end{aligned} \tag{2.26}$$

which agrees with Ref. [14] when the system possesses C_2^z symmetry such that $\tau_1 = \tau_2$, $\tau_3 = \tau_4$.

Let us now consider the consequences of this expression on frequencies of full reflection and full transmission.

For full transmission, we require $T = 1$ and thus $R = 0$. Comparing to Eq. (2.25) shows that

$$\frac{1}{\sigma} = \frac{1}{\tau_1} - \frac{1}{\tau_4} = 0 \Rightarrow \tau_1 = \tau_4, \tag{2.27}$$

$$\omega - \omega_0 = \pm\frac{1}{r}\sqrt{\frac{4}{\tau_4\tau_2} - \left(\frac{1}{\tau_2} + \frac{1}{\tau_4}\right)^2 r^2}, \tag{2.28}$$

so full transmission occurs when the decay rates are effectively P-symmetric. For a structure that possesses P-symmetry, this condition is automatically guaranteed, and indeed we observe that transmission reaches unity near the Fano resonance, see Fig. 2-2.

For full reflection, we require $R = 1$. Eq. (2.25) imposes the condition

$$\left[r(\omega - \omega_0) \pm \sqrt{\frac{4}{\tau_1\tau_2} - \frac{r^2}{\tau^2} - \frac{2}{\tau\sigma} - \frac{1}{\sigma^2 r^2}}\right]^2 + \left(\frac{1}{\sigma r}\right)^2 = (\omega - \omega_0)^2 + \frac{1}{\tau^2}. \tag{2.29}$$

The discriminant of this equation is

$$4\left(\frac{4}{\tau_1\tau_2} - \frac{r^2}{\tau^2} - \frac{2}{\tau\sigma} - \frac{1}{\sigma^2 r^2}\right) - 4(1 - r^2)\left(\frac{1}{\tau^2} - \frac{1}{\sigma^2 r^2}\right) = -4\left(\frac{1}{\tau_1} - \frac{1}{\tau_2}\right)^2, \tag{2.30}$$

so full reflection is possible when the discriminant is non-negative, i.e. when the decay rates are effectively z-symmetric: $\tau_1 = \tau_2$. For a structure that possesses z-symmetry, this condition is guaranteed, as discussed in Ref. [14].

2.3 General Bounds on Asymmetric Coupling Rates

2.3.1 Analytical Results

We now derive bounds on the achievable asymmetry of coupling to the top and bottom based on Eqs. (2.10,2.11) derived from time-reversal symmetry.

Denoting the emission ratio as $|d_4/d_2| = a_r$, $|d_3/d_1| = a_l$, by taking the ratio of

the time-reversal symmetry equations we find

$$a_l^2 = \left|\frac{jt + ra_r e^{j\theta}}{r + jta_r e^{j\theta}}\right|^2 = \frac{t^2 + r^2 a_r^2 + 2tra_r \sin\theta}{r^2 + t^2 a_r^2 - 2tra_r \sin\theta}, \tag{2.31}$$

thus giving a bound

$$\left|\frac{t - ra_r}{r + ta_r}\right| \leq a_l \leq \left|\frac{t + ra_r}{r - ta_r}\right|. \tag{2.32}$$

Therefore, the amount of achievable asymmetry to top and bottom on the left is bound by that on the right, and vice versa.

If we make the assumption of C_2^z symmetry, the two channels on the top and bottom would be constrained to have the same coupling rates, and hence $d_1 = d_2$, $d_3 = d_4$. Plugging this into Eq. (2.10), we have

$$e^{j\phi}(rd_1^* + jtd_3^*) + d_1 = 0, \tag{2.33}$$

which reduces to the same bound as in Ref. [14]:

$$\sqrt{\frac{1-r}{1+r}} \leq a_l = a_r \leq \sqrt{\frac{1+r}{1-r}}, \tag{2.34}$$

thus demonstrating consistency of our approach. This result can also be obtained from Eq. (2.32) by setting $a_l = a_r$.

Note that in typical photonic crystal systems, at optical frequencies, the index contrast is usually limited to around 3, which limits the interface reflection coefficient to be less than 0.5 for most incident angles, see Fig. 2-3 for a calculation of the interface reflection coefficient based on Fresnel equations. The resulting Fabry-Perot transmittance is given by [19]

$$t^2 = \frac{1}{1 + \frac{4R_0 \sin^2(\delta/2)}{(1-R_0)^2}}, \tag{2.35}$$

where R_0 is the interface reflectance and δ is the phase accumulated when reflecting

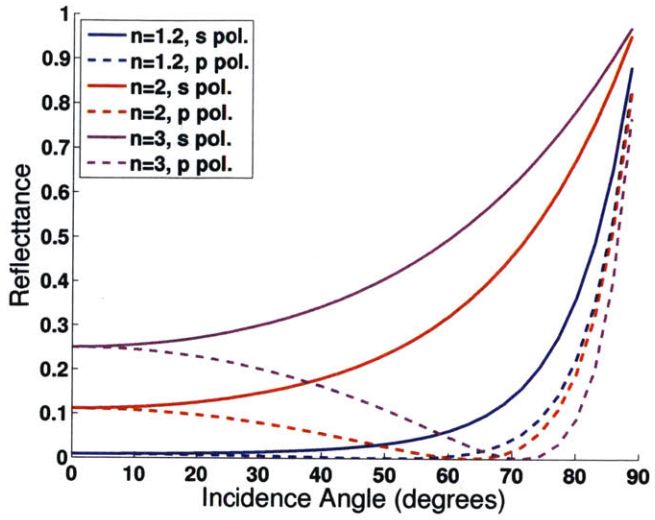

Figure 2-3: Reflectance calculated according to Fresnel equations for light incident from air ($n_0 = 1$) to dielectric.

between the interfaces. This results in the Fabry-Perot direct pathway reflection coefficient $r = \sqrt{1-t^2}$ being considerably smaller than 1, and implies that strong asymmetry in the decay rates to top and bottom is typically difficult to achieve for C_2^z-symmetric structures.

The general bound Eq. (2.32) suggests, however, that much stronger asymmetry can be achieved if we break the C_2^z symmetry of the system. A simplifying case is when the structure possesses inversion symmetry P, as shown in Fig. 2-4. In this case, the decay rates must satisfy $d_1 = d_4$, $d_2 = d_3$, $a_l = 1/a_r$, which would give

$$\frac{\tau_3}{\tau_1} = |\frac{d_1}{d_3}|^2 = |\frac{-re^{j\phi - j\theta_2}}{e^{j\theta_1} + jte^{j\phi - j\theta_4}}|^2 = \frac{1-t^2}{(1+t\cos\phi')^2}, \tag{2.36}$$

where ϕ' is a phase that in general can be tuned through an entire 2π range, and we have defined $\tau_i = |d_i|^2$ to characterize the loss rate. The asymmetry is thus bounded by

$$\sqrt{\frac{1-t}{1+t}} \leq a_l = \frac{1}{a_r} \leq \sqrt{\frac{1+t}{1-t}}, \tag{2.37}$$

where again t is the amplitude transmission coefficient of the direct process governed by the Fabry-Perot cavity response.

For any index contrast, the Fabry-Perot background will always have frequencies with full transmission, thus by appropriate tuning of the resonance frequency, the lower and upper bounds of Eq. (2.37) approach 0, $+\infty$. Moreover, since the bound above originates from taking the norm of a complex quantity, this bound should be saturated for appropriate choices of structural parameters and wavevector, resulting in highly asymmetric decay rates of the photonic structure to top and bottom directions.

For some practical devices, we cannot neglect the $\vec{k}'_{\parallel} = -\vec{k}_{\parallel}$ vector that has an opposite momentum, and should consider the total asymmetry ratio after taking both sides into account. Using the expression $|d_1|^2 + |d_3|^2 = |d_2|^2 + |d_4|^2$ resulting from the time-reversal-pair relation between the resonances, the total asymmetric ratio can be written as

$$a^2 = \frac{|d_3|^2 + |d_4|^2}{|d_1|^2 + |d_2|^2} = \frac{a_r^2 + a_l^2 + 2a_l^2 a_r^2}{a_l^2 + a_r^2 + 2}, \tag{2.38}$$

where a_l and a_r satisfy the bound specified in Eq. (2.32). Taking the partial derivative of the above equation with respect to a_l^2 yields

$$\frac{\partial}{\partial(a_l^2)}\left(\frac{a_r^2 + a_l^2 + 2a_r^2 a_l^2}{a_r^2 + a_l^2 + 2}\right) = \frac{2(a_r^2+1)^2}{(a_l^2 + a_r^2 + 2)^2} > 0, \tag{2.39}$$

so to maximize the asymmetric ratio requires minimizing a_l within the bounds. We thus plug in the lower bound of Eq. (2.32) into Eq. (2.38), which gives

$$\begin{aligned} a^2 &= \frac{a_r^2 + (\frac{t+ra_r}{r-ta_r})^2 + 2}{a_r^2 + (\frac{t+ra_r}{r-ta_r})^2 + 2a_r^2(\frac{t+ra_r}{r-ta_r})^2} \\ &= \frac{(a_r^2+2)(r-ta_r)^2 + (t+ra_r)^2}{a_r^2(r-ta_r)^2 + (2a_r^2+1)(t+ra_r)^2}. \end{aligned} \tag{2.40}$$

Taking the derivative of the above expression with respect to a_r, we find

$$\frac{d(a^2)}{d(a_r^2)} = \frac{-8a_r + 8t^2 a_r + 4tr(a_r^2 - 1)}{(2tra_r + 2a_r^2 - t^2(a_r^2-1))^2}, \tag{2.41}$$

which reaches extrema at $a_r^2 = (r \pm 1)/t$. Retaining the physical solution (+ sign), the maximal amount of asymmetry is attained when $a_l^2 = a_r^2 = (r+1)/t$. This suggests that the maximal amount of top-down asymmetry still observes the bound presented in Eq. (2.34).

Note that it is not straightforward to lump all channels with radiation in the top direction into a single port and all channels in the bottom direction into another single port to obtain this result: the coupling coefficients to the left and right can in general be different. Our results confirm, however, that even if one allows the general situation of breaking C_2^z symmetry of the system, if the left and right channels are excited equally then the same bound as a C_2^z-symmetric structure will apply to the total asymmetry.

Our derivation relies on the assumption of time-reversal symmetry and energy conservation, so one possibility to go beyond this bound of total coupling is to relax these assumptions and generalize TCMT to cases with magneto-optical effects and/or gain and loss, as well as cases where the substrate and superstrate are different. A more practical way to get around this might be to employ side-coupling or laser pumping, in which the incident light imposes a certain $\vec{k}_{\|}$ to the system.

2.3.2 Comparison to Simulations

To verify these analytical results, we performed numerical simulations using the finite difference time domain (FDTD) method [20] with the freely available software package MEEP [21]. Harmonic inversion [22] and far field amplitude analysis are used to determine the coupling rates to top and bottom for each resonance. We place reference planes in the far field, between the structure and the perfectly matched layers (absorbs outgoing waves), and integrate the Bloch wave functions over a unit cell on this plane, as described in Ref. [23]. This gives a complex vector (c_x, c_y) containing amplitude and phase information of the coupling rates. We examine the amplitude to determine the asymmetry of the coupling rates, but the phase variation across different $\vec{k}$-vector points also contains interesting information in connection to bound states in the continuum.

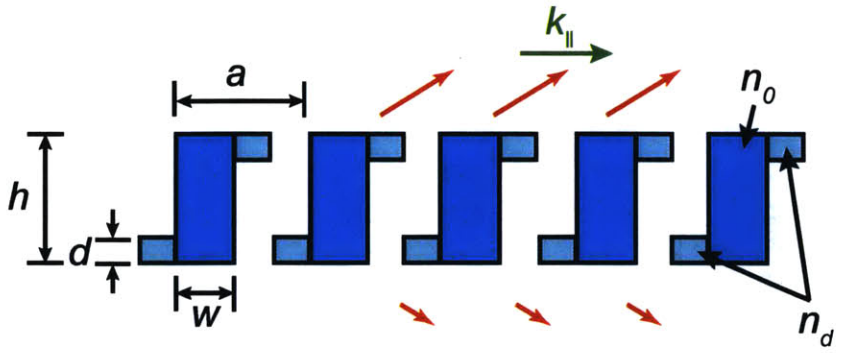

Figure 2-4: Specific P-symmetric structure that we use in our numerical examples and relevant parameters. a: periodicity of photonic crystal, h: height of central slab, w: width of central slab, n_0: refractive index of central slab, d: height of additional pieces on the sides (the width of the additional pieces is $(a-w)/2$), n_d: refractive index of additional pieces on the sides.

To compare to the bound given by Eq. (2.37), we use plane wave excitation to determine the transmission and reflection spectrum for different frequencies and wavevectors, and fit the Fabry-Perot background away from the resonance to determine the background transmittivity. Due to the differences between discretization schemes in various software packages, we used MEEP for both resonance calculations and transmission spectrum calculations. Convergence for transmission spectra near resonances is relatively poor in MEEP, so we use narrow-band excitations of width $\Delta\omega = 0.01 \times 2\pi c/a$ to excite plane waves and discard data close to the resonance. We vary the refractive index, height and width of the dielectric and optimize the maximal asymmetric coupling with respect to wavevector for each structure; see Fig. 2-4 for a schematic of our simulation parameters.

The results are given in Fig. 2-5, where each data point in the figure represents the maximal asymmetric coupling point, optimized over choices of in-plane momentum $\vec{k}_{\|}$, for various structure parameters. We can clearly see that all data points observe the bound Eq. (2.37) derived above, for asymmetric ratios ranging from 1 (no asymmetry) to 10^3 and beyond (strong asymmetry). Moreover, for each value of the background transmission coefficient, by appropriate optimization of the structural parameters and in-plane momentum, this bound can be saturated. The crosses that do not saturate

the bound are structures with very little perturbation from z-mirror symmetric due to our parameter choices.

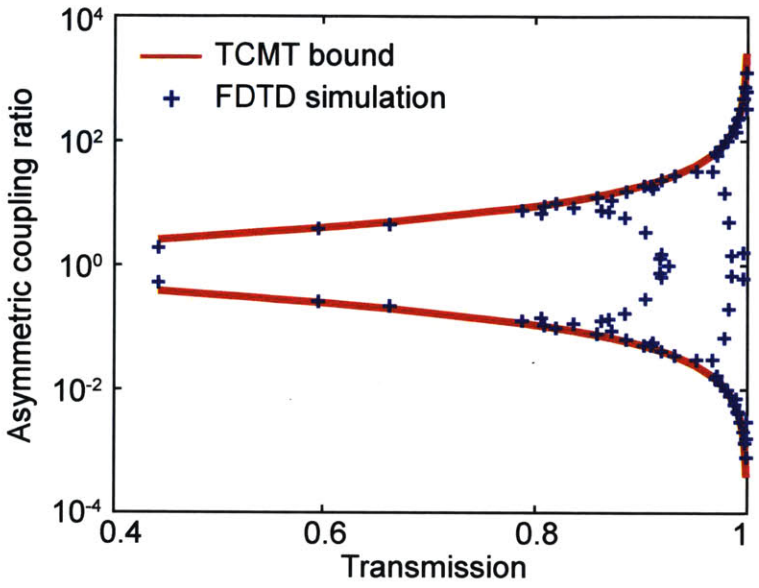

Figure 2-5: Numerical verification of bounds of asymmetry for P-symmetric structures, derived using TCMT. Lines indicate bounds derived from TCMT. Each cross indicates simulation results of the maximum asymmetry for a given structure, optimized over in-plane momentum. The transmittivity t is fitted from the Fabry-Perot background, and the asymmetric coupling ratio is calculated from the Poynting flux in the top and bottom directions.

2.4 Examples of Highly Asymmetric Coupling

In this section, we provide detailed examples of the strong asymmetry that can be achieved, guided by the bounds derived above. As the form $(1+t)/(1-t)$ (P-symmetric structure) of the bound suggests, strong asymmetry can be achieved when the resonance frequency is tuned to coincide with locations of large transmittivity on the Fabry-Perot background. Note that this can be achieved for general refraction indices, since the Fabry-Perot background always has many frequencies of full transmission (separated by the so-called free spectral range).

We optimize over the structural parameters shown in Fig. 2-4 to find examples of

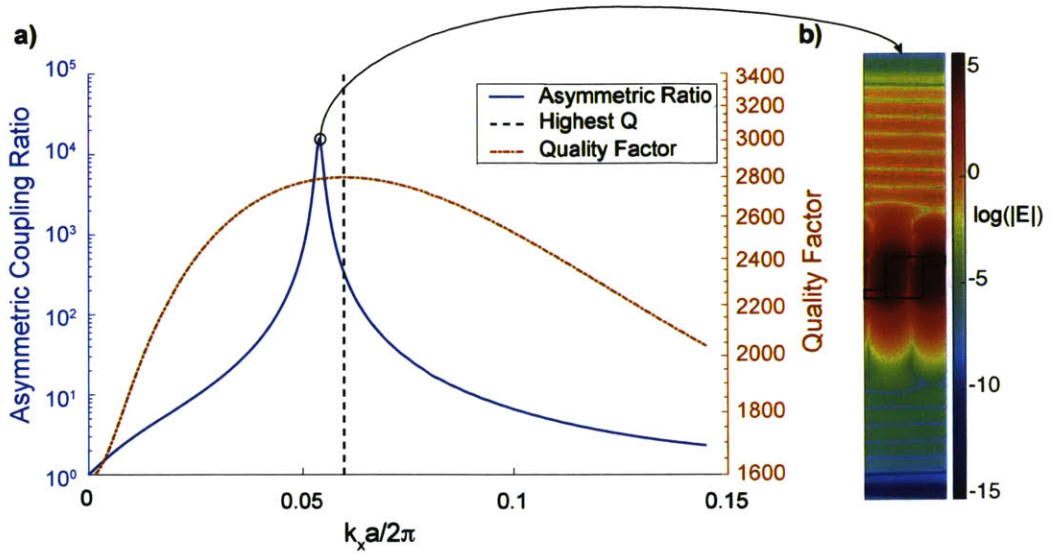

Figure 2-6: Strong asymmetric coupling over a range of momenta, including the point of highest quality factor. Left: plot of asymmetric ratio and quality factor as a function of k_x, along the $k_y = 0$ axis in momentum space; Right: log scale plot of field intensity at highest asymmetry point, clearly demonstrating the strong asymmetry of the coupling to top and bottom.

high asymmetry in coupling to the top and bottom radiation continua. This example consists of the second TM polarization band of a 1D photonic crystal with structural parameters $a = 1$ (by scale invariance of the Maxwell's equations, we can set this to 1 in our simulations), $h = 1.5$, $n_0 = n_d = 1.45$, $d = 0.3$ as defined in Fig. 2-4, and the resulting asymmetric ratio and quality factor as a function of in-plane k_x, along with the radiation field distribution at maximal asymmetry, are shown in Fig. 2-6. The resonance frequency lies very close to a point of full transmission on the Fabry-Perot background, and exhibits an asymmetry exceeding 10^4 at the $\vec{k}_{\|}$ point of largest asymmetry as well as an asymmetry over 300 at the point of highest quality factor. It may therefore be possible to produce a laser that preferentially emits to the top or bottom using the basic principles discussed above.

Another interesting application of our results is for rapid steering of the direction of light emission by slight tuning of the frequency. This could be useful, for example, for applications such as Light Detection and Ranging (LIDAR) [24] or antennas.

We design such a structure by perturbing a bound state in the continuum (BIC) [23, 25, 26]. BICs are localized solutions embedded in the radiation continuum, where due to destructive interference of the amplitude for decay between outgoing wave channels, the quality factor (Q) of a resonance above the light line approaches infinity. In previous work [23, 25, 26], the photonic structures are chosen to be symmetric in z, and symmetry and topology arguments guarantee the existence of BICs [23]. In the case of broken z-mirror symmetry, the quality factor will be finite but still very high. We expect that this symmetry breaking will also split the momenta where interference cancellation occurs towards the top and bottom of the slab, thereby creating strong asymmetry in the two directions, with the extrema separated only by a small $\vec{k}_{\|}$. The perturbation here is P-symmetric, thereby satisfying the conditions given above in section 2.3.1, but it breaks mirror symmetry in the z-direction.

Based on the example in Fig. 3 of Ref. [23], we choose $h = 1.5$, $n_0 = 1.45$, $d = 0.1$, $n_d = 1.1$, again examining the second TM band. The resulting asymmetric ratio and frequency as a function of in-plane k_x are shown in Fig. 2-7. The asymmetric ratio can be flipped from predominantly radiating to the top to mostly radiating to the bottom (by a factor of 10^4) by changing k_x by as small as $0.05 \times 2\pi c/a$ or equivalently, by changing the frequency by $3 \times 10^{-4} \times 2\pi c/a$. The radiative quality factor of these resonances are on the order of 10^6, so these two bands will be well-separated in emission. One can thereby envision rapid tuning of the emission direction by changing the frequency of radiation slightly, which could be useful for antenna or LIDAR applications.

Finally, we give an example where there are multiple peaks of highly asymmetric coupling across the Brillouin zone. Choosing $a = 1$, $h = 1.5$, $w = 0.45$, $d = 0.5$, $n_0 = 1.45$, $n_d = 1.15$, the asymmetric ratio of the second TM band across the Brillouin zone is shown in Fig. 2-8. There are multiple peaks of strong asymmetry that appear across the Brillouin zone, in both directions. This example shows that many different distributions of high asymmetry peaks can be generated by appropriate choices of parameters.

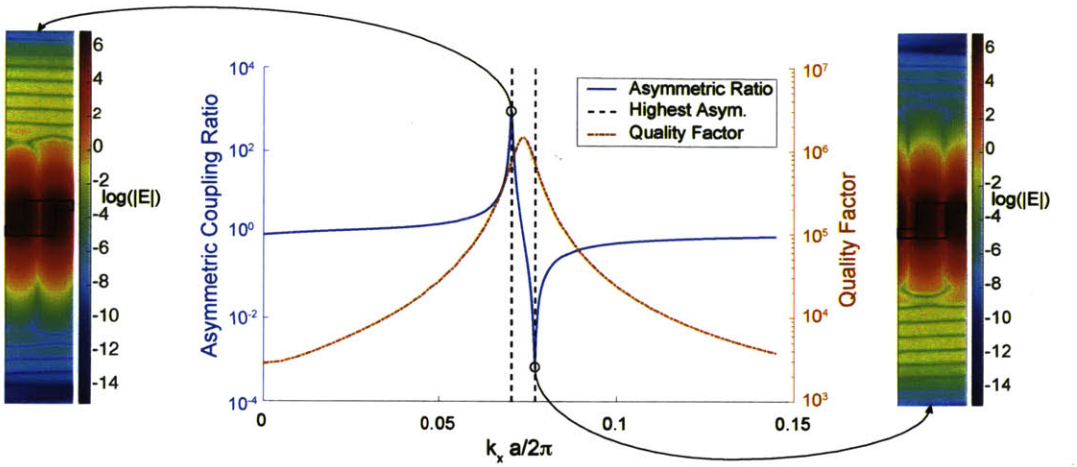

Figure 2-7: Rapid switching of asymmetric direction by tuning frequency or in-plane momentum. Left and right: log scale plot of field intensity showing coupling to top or bottom only at certain $\vec{k}$-points. Middle: plot of the asymmetric ratio and quality factor as a function of k_x, along the $k_y = 0$ axis in momentum space.

2.5 Experimental Considerations and Perspectives

In the preceding sections, we have derived a TCMT formalism to understand the coupling of photonic crystal slabs to arbitrary in-plane $\vec{k}$-vectors, and used this formalism to derive a bound on the achievable asymmetric coupling from photonic crystal slabs. Examples of strong asymmetry have also been given guided by these design principles.

Fabrication of photonic crystal slabs often uses electron beam lithography with reactive ion etching, interference lithography [5], or nanoimprint technology [27]. These methods generally approach the sample from above, resulting in straight vertical walls in the fabricated devices. For our proposed devices that break z-mirror symmetry while preserving inversion symmetry, other fabrication methods will be required. One possibility would be to use focused ion beam milling to produced slanted walls [28]. Recently developed technologies such as angled-etching [29] are also a feasible alternative, but more detailed calculations of the tilted holes produced via this method will be required to design an asymmetrically emitting device.

For laser applications [8], it is important to address the symmetry between $\vec{k}_{\|}$ and $-\vec{k}_{\|}$. In a system with inversion symmetry, the emission to the top at $\vec{k}_{\|}$ and

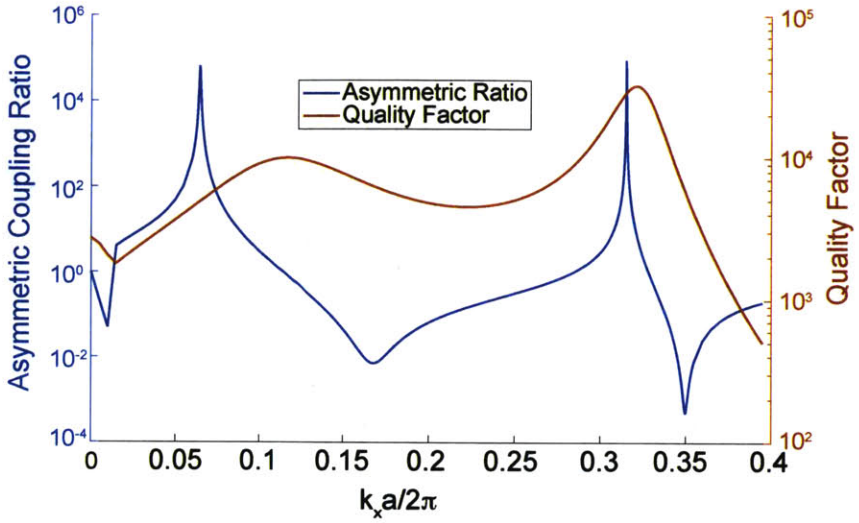

Figure 2-8: Multiple points of high asymmetry appearing across the Brillouin zone. Plot of the asymmetric ratio and quality factor as a function of k_x, along the $k_y = 0$ axis in momentum space.

to the bottom at $-\vec{k}_{\|}$ will be of equal magnitude, which implies that although for a fixed $\vec{k}$-vector we have achieved strong asymmetry, for an actual laser we still need some mechanism to separate the pairs of $\vec{k}$-vectors related by inversion/time-reversal symmetry. One possibility is to operate in an amplifier mode, in which an incoming seed laser stimulates laser emission; due to the properties of stimulated emission, the photons produced must be identical to the incoming ones and thus have the same $\vec{k}_{\|}$, thereby separating the pairs of modes. Another possibility is to use a tilted pump profile (either on-resonance optical pumping or electrical gating) that breaks inversion symmetry, thus enabling preferential lasing of one mode.

Another important question that will need to be addressed is control of the $\vec{k}$-point of lasing and achieving strong asymmetry at this particular point. Generally, lasing will occur in the direction of highest total quality factor. We have demonstrated that asymmetric coupling ratios as large as 300 can be achieved at the point of highest quality factor, but the quality factor profile is relatively flat around the neighborhood. An alternative way to achieve lasing at the desired $\vec{k}$-point is to use other dissipation

channels to control the total quality factor. The transverse quality factor resulting from the finite boundary area of the photonic structure may often provide a larger contribution to the total decay, and by engineering the group velocity by band folding techniques [30], it may be possible to move the lasing mode to a point of stronger asymmetry.

For grating couplers, other factors such as mode matching with the optical fiber that light will be coupled to, as well as reflection back into the waveguide, both need to be taken care of. Mode matching can be achieved by chirping the lattice parameters such that the quality factor further along the waveguide is smaller, thereby emitting the same total amount of light; reflections are already partially mitigated by tilted walls, and further impedance matching could help to reduce such loss. However, more extensive numerical optimization and FDTD simulations will be required, and for CMOS-compatible platforms the effect of substrates also needs to be incorporated into our formalism.

While the bounds corresponding to $(1+t)/(1-t)$ have been derived under the assumption of an inversion-symmetric structure, it might also be possible to engineer such strong asymmetries in a structure that does not retain this symmetry. It will be interesting to explore more deeply the possibilities for achievable asymmetry in such a more general setting and demonstrate strong asymmetry for more general device configurations.

Chapter 3

Topological Half Charges in the Radiation Polarization of Photonic Crystal Slabs

3.1 Background and Motivation

Generating and controlling light with interesting structures and topology is appealing for both gaining better fundamental understandings of light and employing light in real-world applications. From a fundamental physics point of view, the ability to engineer interesting phase fronts and polarization topologies reveals the rich possibilities in electromagnetics, while for practical applications, nontrivial light polarizations can be used to encode information or optically fabricate microstructures with novel topologies.

Early interest in structured light began from the discovery of orbital angular momentum (OAM) of light [31, 32]. These are Laguerre-Gaussian solutions to Maxwell's equations that have a winding phase front, and can be used to produce torques in nanoscale machines [33], control and manipulate nanoparticles in optical tweezers [34], and generate qudits for quantum communication [35]. Another interesting direction in understanding structured light are vector beams [4] with spatially varying

polarization configurations. These vector beams can exhibit sharper focusing [36], and may also be useful for laser machining applications [37].

Cylindrical vector beams, in which the polarization is cylindrically symmetric, have been extensively studied [4]. However, the cylindrical symmetry requires that the winding of polarization around the singularity must be an integer. More recently, half-integer topological charges, corresponding to Mobius strips of light polarization, have been suggested [38] and experimentally demonstrated [39]. The polarization Mobius strip originates from the interference between two Laguerre-Gaussian beams, and is mapped out using nanoparticle scattering under a microscope.

Previously, vector beams have been generated using axial birefringence [40] and dichroic materials, liquid crystal phase plates (q-plates) [41], multimode step-index fibers [42] and glass cones [43]. However, many of these generation schemes generally require special materials, and are sometimes challenging for integration and control.

Recent advances in the field of topological photonics [44] and non-Hermitian photonics [45, 46], on the other hand, have introduced intriguing mathematical ideas to understand and engineer optical phenomena. Periodic structures such as photonic crystals allow the engineering of band structures, which can exhibit topological features, and the coupling to the radiation continuum of slabs allows a natural realization of non-Hermitian physics. One advantage of these designs is that they are material independent, employ the simplest dielectric formalisms, yet still reveal interesting topological behavior. Such structures can be easily fabricated over large scales using techniques such as interference lithography. It would therefore be interesting to demonstrate the generation of vector beams from photonic crystal structures.

Bound states in the continuum (BICs), briefly discussed in the preceding chapter, in fact correspond to integer-charge vector beams [23]. These BICs are formed by the intersection of lines where the x and y polarizations equal zero respectively. The polarization winds around the BIC (see for instance Fig. 1(c) of Ref. [23]), and the charge of the vector beam is equal to the topological charge of the BIC. Such integer vector beams can easily be generated with photonic crystal slabs made out of regular dielectric materials, eliminating the need for q-plates or spatial light modulators.

However, previous work has only examined integer topological charges.

In this chapter, we demonstrate that light emission from photonic crystal slabs can also be tailored to form a polarization Mobius strip. This half-integer topological charge arises from the π Berry phase associated with one Dirac point, or two exceptional points. To verify the existence of polarization Mobius strips, we propose to image the polarization along isofrequency contours using scattered light from photonic crystal slabs.

3.2 Analytical Two Band Model for Exceptional Points

In this section, we consider a simple analytical model for the band structure near the Γ point, at a frequency close to a symmetry-protected quadratic degeneracy point. We shall start from symmetry considerations to write down a Hamiltonian for the two degenerate modes in the absence of symmetry breaking [47], then add in symmetry breaking terms and differential loss and analyze the eigenvalue spectrum. We shall see the emergence of exceptional points [48, 49] when system symmetries are broken, and connect them to topological characteristics of the system.

3.2.1 Basic Symmetry Arguments

Symmetry is a powerful tool to help understand features such as degeneracies and interactions between bands in photonic crystals. More formally, the language of group representation theory [50] is employed to classify the symmetry of modes.

The most common types of photonic crystal lattices are square lattices and hexagonal lattices, the former having a C_{4v} symmetry group and the latter having a C_{6v} symmetry group, see Fig. 3-1. Both of these groups have two-dimensional irreducible representations (irreps), and the modes corresponding to these irreps will be doubly degenerate at $\vec{k}$-points that preserve the symmetries. This implies that if the structure has C_{4v} or C_{6v} symmetry, then there may exist doubly degenerate modes at the Γ, M or K (retains C_{3v} symmetry, which also has a 2D irrep) point. Some examples include the third/fourth TE band at the Γ point for the square lattice or hexagonal

lattice [51].

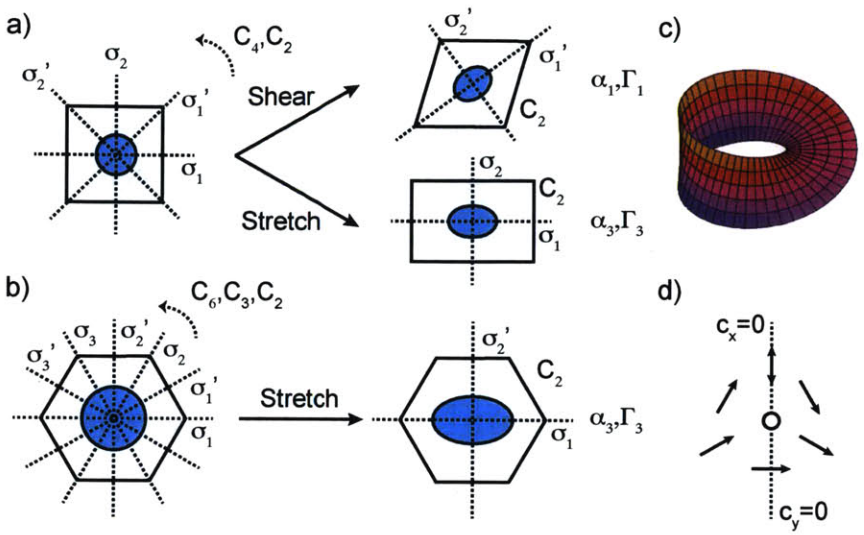

Figure 3-1: Schematic for (a) square lattice (C_{4v}) and (b) hexagonal lattice (C_{6v}) symmetry groups and symmetry breaking operations we consider, as well as (c) a Mobius strip (adapted from Wikipedia) and (d) a polarization Mobius strip, where we return to the opposite orientation after looping around the center.

We shall consider modes in the vicinity of the Γ point, since it will be easier to observe the band structure near this point with far-field measurements, although the discussion is similar for the M point [47] and K point [52].

Following the discussion of Chong et al. [47], we expand the Bloch wave function in terms of the two degenerate bands $u^1(\vec{r})$ and $u^2(\vec{r})$ near the Γ point. For small $\vec{k}$, the wave function can be expanded as

$$u_k^1(\vec{r}) = c_{11}(\vec{k})u^1(\vec{r}) + c_{12}(\vec{k})u^2(\vec{r}), u_k^2(\vec{r}) = c_{21}(\vec{k})u^1(\vec{r}) + c_{22}(\vec{k})u^2(\vec{r}), \tag{3.1}$$

where $H(\vec{k})u_k^i(\vec{r}) = \lambda_i(\vec{k})u_k^i(\vec{r})$, with $i = 1, 2$.

Under an operation g that belongs to the symmetry group, the Hamiltonian must transform as

$$D(g)H(\vec{k})D^{-1}(g) = H(g\vec{k}), \tag{3.2}$$

where $D(g)$ falls under a 2D irrep corresponding to the degeneracy. By enumerating the lowest order terms that can contribute and imposing symmetry constraints, we can write down the Hamiltonian $H_0(\vec{k})$ when the lattice symmetry is not broken. We can then consider particular types of lattice symmetry breaking, and write down expressions for $H(\vec{k})$ that obey the remaining symmetries. In the following, we discuss two separate cases: small perturbations to a square lattice, and to a hexagonal lattice, both near the Γ point.

Observing the resulting emission is easiest when the photonic crystal slab is fabricated in large area. Such large area fabrication is often achieved via interference lithography, where the intensity modulation due to interference between two laser beams defines the pattern. Stretching the lattice can be achieved by tilting the out-of-plane angle of laser beams to change the in-plane periodicity, and shearing the lattice can be achieved by changing the in-plane relative angle of the laser beams, but other types of symmetry breaking are more challenging. We will therefore focus on symmetry breaking terms consistent with experimental fabrication constraints, as shown in Fig. 3-1.

3.2.2 Perturbing a Square Lattice

This case follows the discussion in Ref. [47]. The square lattice has a C_{4v} symmetry, and the unique 2D irrep corresponds to rotation matrices. By writing down the rotation matrices in terms of Pauli matrices σ_i and considering how they act on k_x, k_y, one obtains the following Hamiltonian:

$$H_{4v}(k_x, k_y) = \omega_0 - i\Gamma_0 + \lambda_0[\sum_{i\in\{x,y,z\}} (\alpha_i + i\Gamma_i)\sigma_i + \beta(k_x^2 - k_y^2)\sigma_z + 2k_xk_y\sigma_x + \gamma(k_x^2 + k_y^2)], \tag{3.3}$$

where ω_0 is a reference frequency, Γ_0 is the average decay rate of the two bands, λ_0 is a scale factor, β and γ control the curvatures of the band, and α_i and Γ_i correspond to different ways of partially breaking the symmetry of the lattice, with α_i describing the difference in frequency and Γ_i describing the difference in decay rate. α_1 (Γ_1)

	E	C_6	C_6^{-1}	C_3	C_3^{-1}	C_2
E_1	I	$\frac{I}{2}+\frac{\sqrt{3}}{2}i\sigma_y$	$\frac{I}{2}-\frac{\sqrt{3}}{2}i\sigma_y$	$-\frac{I}{2}+\frac{\sqrt{3}}{2}i\sigma_y$	$-\frac{I}{2}-\frac{\sqrt{3}}{2}i\sigma_y$	$-I$
E_2	I	$-\frac{I}{2}+\frac{\sqrt{3}}{2}i\sigma_y$	$-\frac{I}{2}-\frac{\sqrt{3}}{2}i\sigma_y$	$-\frac{I}{2}-\frac{\sqrt{3}}{2}i\sigma_y$	$-\frac{I}{2}+\frac{\sqrt{3}}{2}i\sigma_y$	I
	σ_1	σ_1'	σ_2	σ_2'	σ_3	σ_3'
E_1	σ_z	$\frac{1}{2}\sigma_z+\frac{\sqrt{3}}{2}\sigma_x$	$-\frac{1}{2}\sigma_z+\frac{\sqrt{3}}{2}\sigma_x$	$-\sigma_z$	$-\frac{1}{2}\sigma_z-\frac{\sqrt{3}}{2}\sigma_x$	$\frac{1}{2}\sigma_z-\frac{\sqrt{3}}{2}\sigma_x$
E_2	σ_z	$-\frac{1}{2}\sigma_z+\frac{\sqrt{3}}{2}\sigma_x$	$-\frac{1}{2}\sigma_z-\frac{\sqrt{3}}{2}\sigma_x$	σ_z	$-\frac{1}{2}\sigma_z+\frac{\sqrt{3}}{2}\sigma_x$	$-\frac{1}{2}\sigma_z-\frac{\sqrt{3}}{2}\sigma_x$

Table 3.1: Matrices for the two 2D irreducible representations of the symmetry group C_{6v}.

corresponds to shearing the lattice, preserving reflection symmetry with respect to $\kappa_x = \pm\kappa_y$ but breaking the other symmetries; α_2 (Γ_2) corresponds to preserving the rotational symmetry but breaking reflection symmetries; α_3 (Γ_3) corresponds to changing the relative length of the two lattice vectors. There are no first order terms in k_x and k_y due to the remaining symmetries in each of the cases. This Hamiltonian is identical to Eq. (4) of Ref. [47], except that due to a different choice of representation matrices (to be consistent with our discussion of the hexagonal lattice), the Pauli matrices are permuted.

Since ω_0 and Γ_0 correspond to a uniform frequency or decay rate shift, we shall neglect them in the following discussion. The eigenvalues of the remaining part of the Hamiltonian are (using properties of the Pauli matrices simplifies the calculation):

$$E = \gamma(k_x^2+k_y^2) \pm \sqrt{(\alpha_1+2k_xk_y+i\Gamma_1)^2+(\alpha_2+i\Gamma_2)^2+[\alpha_3+i\Gamma_3+\beta(k_x^2-k_y^2)]^2}. \tag{3.4}$$

3.2.3 Perturbing a Hexagonal Lattice

The hexagonal lattice also hosts quadratic degeneracies at high symmetry points protected by the 2D irreducible representations. The C_{6v} symmetry group of the hexagonal lattice has two 2D irreps: E_1 corresponds to the rotational group, while E_2 corresponds to transformations on the basis pair x^2-y^2 and $2xy$. Since Pauli matrices form a complete basis for the vector space of 2D Hermitian matrices, we rewrite the representation matrices in terms of Pauli matrices, explicitly given in table 3.1.

We first consider the 2D irrep E_1 corresponding to rotation matrices. Following Eq. (3.2), we consider the symmetry constraints on the form of the Hamiltonian. Generically, the Hamiltonian can be written to second order as

$$H_0(k_x, k_y) = A_0 + A_1 k_x + A_2 k_y + B_1 k_x^2 + B_2 k_x k_y + B_3 k_y^2, \tag{3.5}$$

where A_i and B_i are two-by-two matrices.

In both 2D irreps, the 180° rotation operation C_2 is represented by a matrix proportional to the identity matrix, $D_1(C_2) = -I$, $D_2(C_2) = I$. Operating on the Hamiltonian as in Eq. (3.2), we thus have

$$H_0(k_x, k_y) = H_0(-k_x, -k_y), \tag{3.6}$$

which implies that $A_1 = A_2 = 0$. Indeed, all terms proportional to odd powers of k_x and k_y should vanish.

Reflection σ_1 with respect to the k_x-axis is represented by σ_z in both representations. This implies that

$$\begin{aligned} \sigma_z(B_1 k_x^2 + B_2 k_x k_y + B_3 k_y^2)\sigma_z &= D_i(\sigma_1) H_0(k_x, k_y) D_i(\sigma_1) \\ &= H_0(k_x, -k_y) = B_1 k_x^2 - B_2 k_x k_y + B_3 k_y^2. \end{aligned} \tag{3.7}$$

Any 2×2 matrix can be written as a sum of Pauli matrices and the identity matrix. Using the fact that Pauli matrices commute with themselves and the identity matrix, and anticommute with other Pauli matrices, the preceding equation implies that

$$B_1 = b_{10} I + b_{13}\sigma_z, B_2 = b_{21}\sigma_x + b_{22}\sigma_y, B_3 = b_{30} I + b_{33}\sigma_z. \tag{3.8}$$

Now consider the symmetry requirements imposed by a rotation C_6 of 60°. We first consider the representation E_1 corresponding to rotation matrices. In this case,

we have $D_1(C_6) = (I + \sqrt{3}i\sigma_y)/2$, so that Eq. (3.2) implies

$$(\frac{I}{2} + \frac{\sqrt{3}}{2}i\sigma_y)(B_1k_x^2 + B_2k_xk_y + B_3k_y^2)(\frac{I}{2} - \frac{\sqrt{3}}{2}i\sigma_y)$$
$$= B_1(\frac{1}{2}k_x - \frac{\sqrt{3}}{2}k_y)^2 + B_2(\frac{1}{2}k_x - \frac{\sqrt{3}}{2}k_y)(\frac{\sqrt{3}}{2}k_x + \frac{1}{2}k_y) + B_3(\frac{\sqrt{3}}{2}k_x + \frac{1}{2}k_y)^2. \quad (3.9)$$

Expanding this equation and matching coefficients of k_x^2, we find that

$$b_{10} - \frac{1}{2}b_{13}\sigma_z - \frac{\sqrt{3}}{2}b_{13}\sigma_x = \frac{1}{4}b_{10}I + \frac{1}{4}b_{13}\sigma_z + \frac{\sqrt{3}}{4}(b_{21}\sigma_x + b_{22}\sigma_y) + \frac{3}{4}(b_{30}I + b_{33}\sigma_z). \quad (3.10)$$

Matching coefficients of the Pauli matrices, we arrive at the following relations:

$$b_{10} = b_{30}, b_{13} = -b_{33}, b_{13} = -\frac{1}{2}b_{21}, b_{22} = 0. \quad (3.11)$$

The remaining constraints for coefficients of k_xk_y and k_y^2 are consistent with this and do not impose additional constraints. Therefore, taking out a constant scale factor in front and the shift A_0, the Hamiltonian for a quadratic degeneracy corresponding to the E_1 representation of the C_{6v} group can be written as

$$H_{0,6v1}(k_x, k_y) = \omega_0 - i\Gamma_0 + \lambda_0[-(k_x^2 - k_y^2)\sigma_z + 2k_xk_y\sigma_x + \gamma(k_x^2 + k_y^2)] \quad (3.12)$$

Due to fabrication constraints, we consider only symmetry breaking terms that correspond to the group C_{2v}, i.e. terms that preserve 180° rotational symmetry and contain two reflection planes. This implies that Eqs. (3.6,3.7) still hold, so that the symmetry breaking term can only contain I and σ_z. The former corresponds to a uniform shift which is irrelevant, while the latter can be incorporated into the Hamiltonian to arrive at the general form for the E_1 representation

$$H_{6v1}(k_x, k_y) = \omega_0 - i\Gamma_0 + \lambda_0[(\alpha_3 + i\Gamma_3)\sigma_z - (k_x^2 - k_y^2)\sigma_z + 2k_xk_y\sigma_x + \gamma(k_x^2 + k_y^2)] \quad (3.13)$$

In the preceding parts we have imposed constraints corresponding to C_6 and σ_1. These are generators of the C_{6v} group, so a Hamiltonian that transforms correctly under these group operations is guaranteed to transform correctly under an arbitrary operation in C_{6v}.

A similar discussion for the E_2 representation of the C_{6v} group replaces $D_1(C_6) = (I + \sqrt{3}i\sigma_y/2)$ by $D_2(C_6) = (-I + \sqrt{3}i\sigma_y)/2$, and arrives at the constraints

$$b_{10} = b_{30}, b_{13} = -b_{33}, b_{13} = \frac{1}{2}b_{21}, b_{22} = 0, \tag{3.14}$$

resulting in the Hamiltonian for the E_2 representation

$$H_{6v2}(k_x, k_y) = \omega_0 - i\Gamma_0 + \lambda_0[(\alpha_3 + i\Gamma_3)\sigma_z + (k_x^2 - k_y^2)\sigma_z + 2k_xk_y\sigma_x + \gamma(k_x^2 + k_y^2)]. \tag{3.15}$$

Comparing to the Hamiltonian for the square lattice, we see that the main difference for the hexagonal lattice is to impose a fixed value of the parameter β to be ± 1 in the model. This corresponds to the fact that the hexagonal lattice is more isotropic in different directions.

3.2.4 Exceptional Points and Half Charges

Due to fabrication considerations (interference lithography, as discussed below in section 3.6), we shall only consider symmetry breaking with nonzero α_1 or α_3. One important feature that appears in the presence of these symmetry breaking terms and loss is the exceptional point (EP) [48, 53, 54], in which both the eigenvalues and eigenvectors coincide at a particular $\vec{k}$-point. At this point, the Hamiltonian matrix becomes defective, and the remaining eigenfunction becomes orthogonal to itself under the unconjugated inner product [53, 55]. Close to a second-order EP (two eigenvectors coalesce), in one direction the frequency is roughly constant and the decay rates of the two bands split with a square-root scaling, while in the opposite direction the decay rates are roughly constant and the frequencies split with a square-

root scaling. Such a structure exemplifies the non-Hermitian nature of the system. Mathematically, the EP will occur when the square root term in Eq. (3.4) vanishes, so that

$$[\alpha_3 + i\Gamma_3 + \beta(k_x^2 - k_y^2)]^2 + (2k_xk_y + \alpha_1 + i\Gamma_1)^2 = 0. \tag{3.16}$$

Equating the real and imaginary parts of this equation to zero yields

$$\alpha_1 + 2k_xk_y = \Gamma_3, \quad \alpha_3 + \beta(k_x^2 - k_y^2) = -\Gamma_1, \tag{3.17}$$

or

$$\alpha_1 + 2k_xk_y = -\Gamma_3, \quad \alpha_3 + \beta(k_x^2 - k_y^2) = \Gamma_1, \tag{3.18}$$

which can be solved to give

$$k_x^2 = \frac{-(\alpha_3 + \Gamma_1) + \sqrt{(\alpha_3 + \Gamma_1)^2 + \beta^2(\Gamma_3 - \alpha_1)^2}}{2\beta}, \quad k_y = \frac{\Gamma_3 - \alpha_1}{2k_x} \tag{3.19}$$

or

$$k_x^2 = \frac{\Gamma_1 - \alpha_3 + \sqrt{(-\alpha_3 + \Gamma_1)^2 + \beta^2(\Gamma_3 + \alpha_1)^2}}{2\beta}, \quad k_y = \frac{-\Gamma_3 - \alpha_1}{2k_x}, \tag{3.20}$$

where we have only chosen the solutions that make k_x and k_y real. In the limit where $\alpha_1 = \pm\Gamma_3$, the above expressions should be understood in terms of a limit using L'Hôpital's rule.

Generally, there will be four such EPs. They can be understood as a consequence of the quadratic degeneracy point splitting into a pair of Dirac points (band-touching points around which the dispersion is linear) under symmetry breaking [47], and each Dirac point splitting into a pair of EPs under the addition of differential loss in the system, see Fig. 3-2 for a schematic.

The existence of EPs can be directly verified by examining the evolution of eigenvalues in momentum space when one adiabatically traverses a loop. If the loop en-

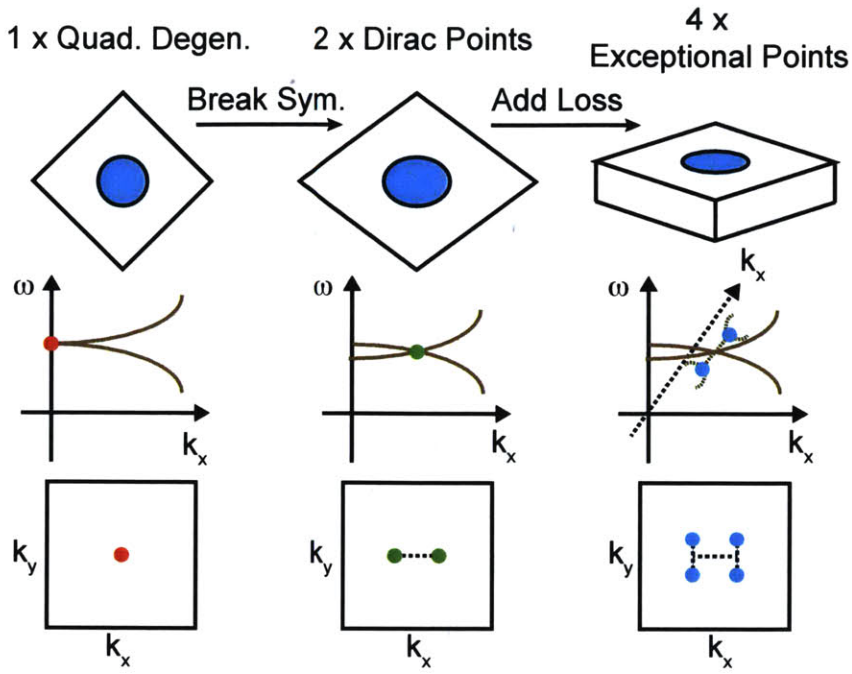

Figure 3-2: Schematic of a quadratic degeneracy point splitting into a pair of Dirac points, and further into four exceptional points.

closes a single EP, then the eigenvalues on the two bands will switch, one of them acquiring an additional π phase shift in the wave function; if two EPs are enclosed, the eigenvalues will return to themselves, but with an additional π phase shift.

In our case, this phase shift can be understood as coming from the π Berry phase associated with a Dirac cone. Close to a Dirac cone, the bands can be described by the Hamiltonian [47]

$$H = k_x\sigma_x + k_y\sigma_y = \begin{pmatrix} 0 & ke^{-i\theta} \\ ke^{i\theta} & 0 \end{pmatrix}. \tag{3.21}$$

We can take the eigenvectors to be

$$|v_1\rangle = \frac{1}{\sqrt{2}}\begin{pmatrix} e^{-i\theta} \\ 1 \end{pmatrix}, |v_2\rangle = \frac{1}{\sqrt{2}}\begin{pmatrix} e^{-i\theta} \\ -1 \end{pmatrix}, \tag{3.22}$$

so the Berry phase on the upper band (the lower band will be analogous), along a

circle enclosing the Dirac point, is given by

$$\gamma = \oint i\langle v_1|\nabla_{\vec{k}}|v_1\rangle d\vec{k} = \int_0^{2\pi} \frac{i}{2}\begin{pmatrix} e^{i\theta} & 1 \end{pmatrix}\cdot\begin{pmatrix} -\frac{ie^{-i\theta}}{k} \\ 0 \end{pmatrix} k d\theta = \pi. \tag{3.23}$$

Under the addition of loss, the bands will only be slightly deformed, and the Berry phase surrounding the pair of EPs will also be π. Therefore, as we adiabatically loop around a pair of EPs, we will pick up a π phase shift when we return to our starting point.

The π phase shift can be viewed as defining a half-integer topological charge: when tracing the polarization vector around a pair of EPs in the far field and returning to the starting point, we have encircled the EPs with a trajectory in momentum space. Along the path, both the polarization direction and phase will wind. Assuming that along the trajectory there are no points of circular polarization (C-points) [56], where the major axis of the polarization ellipse is undefined, the π phase shift corresponds to the direction of the polarization vector flipping when we return to the starting point. This corresponds to a half-integer topological charge, i.e. a Mobius strip [56].

An alternative way to view the half-integer topological charge is from the perspective of nodal lines, i.e. lines where the polarization components c_x or c_y vanish. Along a high symmetry line and upon crossing the Dirac point, we switch from a c_x nodal line to a c_y nodal line. Any other nodal lines will be doubly degenerate by symmetry of the system, hence we have an odd number of c_x and c_y nodal lines entering the isofrequency contours. An inspection of Fig. 3-1(d), where the nodal lines are in the vertical direction, shows that this corresponds to a half-integer polarization winding.

For experimental observation of the topological half-charge, isofrequency contours will be a natural way to map out the polarizations around a pair of EPs. An isofrequency contour is simply a special loop around the EPs, provided that the isofrequency contour is closed, so the preceding discussion about Berry phase and topological charge still holds. Therefore, we can verify the nature of the half-integer topological charge by measurements of the polarization vector along an isofrequency contour.

In view of such measurements, in the following section we shall examine the general shape of isofrequency contours in various parameter regimes using the analytical model. We shall then move on to numerical simulations, first of a 2D photonic crystal infinite in the third direction, to illustrate the properties of the Dirac point, and then present a 3D simulation of a photonic crystal slab with realistic experimental parameters.

We would like to note here that previous work has demonstrated that a Dirac cone at the center of the Brillouin zone with a flat band in the middle can be split under the addition of loss into a ring of exceptional points [57]. In that case, the bands are isotropic in different directions, resulting in a ring instead of a pair of points in particular directions. Moreover, the flat band in the middle results in a trivial Berry phase due to the pseudospin-1 description of the full system [58, 59]. Our system differs here in that the Dirac cone is isolated from any other bands, and thus has a genuine Berry phase winding of π.

3.3 Results from Analytical Model

Using the analytical model above, we can determine the isofrequency contours and exceptional points and model its shape as a function of system parameters. In this section, we discuss various parameter regimes and the corresponding contour shapes. Without loss of generality, we choose $\beta, \gamma > 0$ (a global sign shift with the corresponding α_i takes care of the negative case). Considering realistic experimental implementations, we shall only look at symmetry breaking terms $\alpha_1(\Gamma_1)$ and $\alpha_3(\Gamma_3)$. For simplicity, in this section we shall only consider breaking one symmetry at a time; for a discussion with both terms present simultaneously, see Appendix A.

Depending on the parameter choices, many different types of isofrequency contours can be found. Some characteristic contours that are the most relevant to accessible parameter regimes for experiments are shown here, and more detailed discussions can be found Appendix A. The particular case here with $\beta = \gamma = 0.2$ prior to symmetry breaking most closely corresponds to the lowest symmetry-protected degenerate

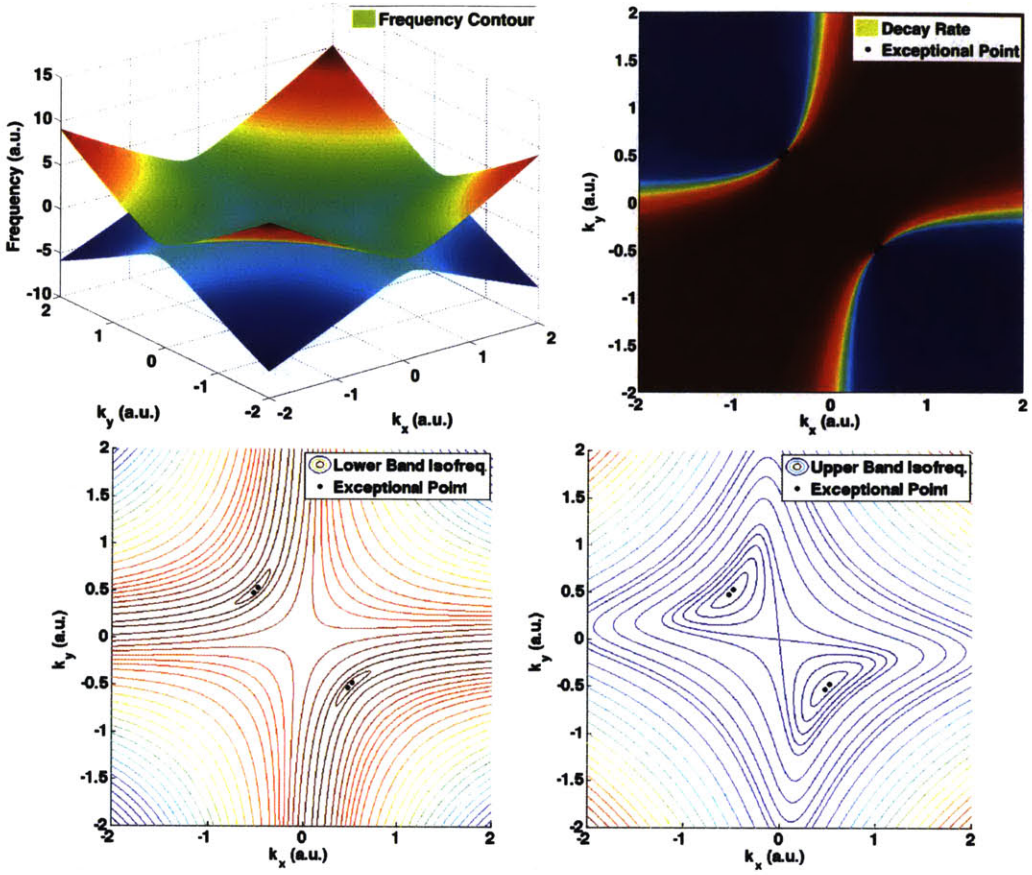

Figure 3-3: Frequency spectrum, isofrequency contours and decay rates for parameter choice $\beta = \gamma = 0.2$, $\alpha_1 = 0.5$, $\Gamma_1 = 0.01$, $\alpha_3 = \Gamma_3 = 0$ in the analytical model.

modes at the Γ point for a square lattice. In this case, the band curvature differences in the $k_x = \pm k_y$ directions are significantly greater than $k_x = 0$ or $k_y = 0$. Note that the isofrequency contours here are not equally spaced in frequency, and are used only for illustration purposes.

In Fig. 3-3, we show an example with parameters $\beta = \gamma = 0.2$, $\alpha_1 = 0.5$, $\Gamma_1 = 0.01$, $\alpha_3 = \Gamma_3 = 0$. The exceptional points are calculated using Eqs. (3.19, 3.20) in the preceding section. On the upper band, we obtain closed, relatively round isofrequency contours containing a pair of EPs. This persists up to the frequency where the isofrequency contours around two different pairs coalesce. On the lower band, due to parameter choices, the isofrequency contours resemble hyperbolas, and extend very far away. The two EPs connect a line of sharp separation between different

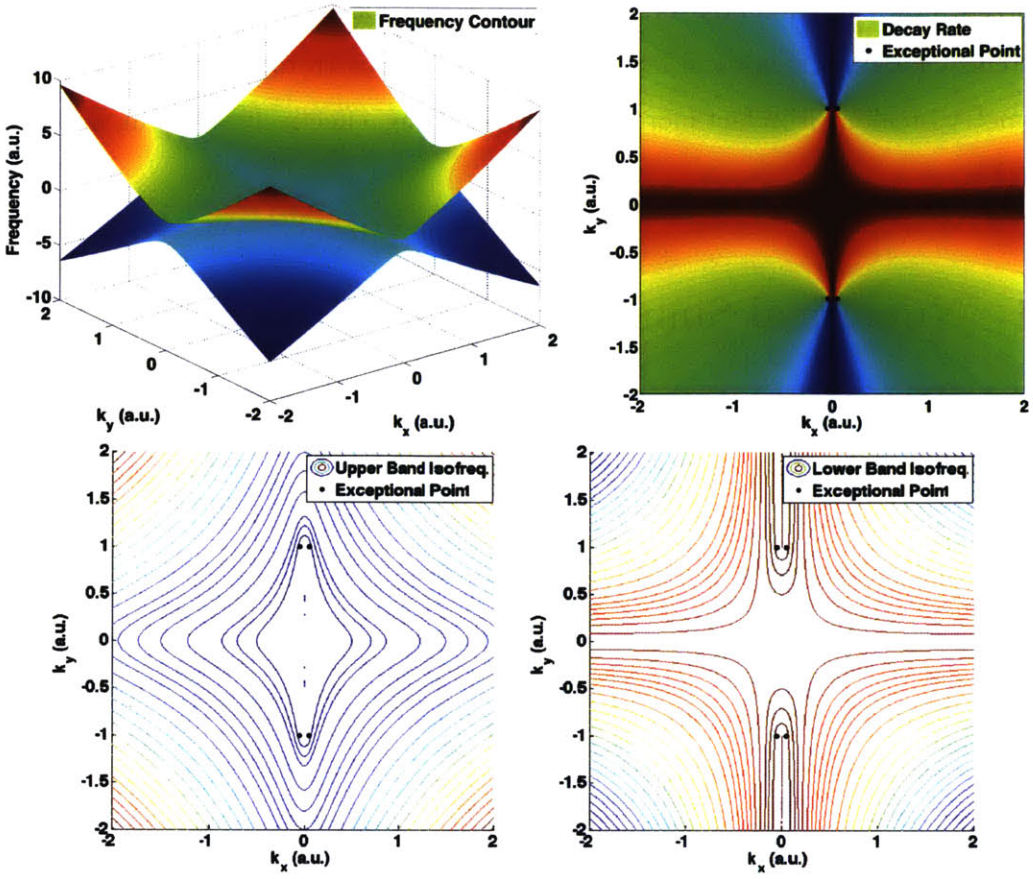

Figure 3-4: Frequency spectrum, isofrequency contours and decay rates for parameter choice $\beta = \gamma = 0.2$, $\alpha_3 = 0.2$, $\Gamma_3 = 0.1$, $\alpha_1 = \Gamma_1 = 0$ in the analytical model.

imaginary part values of the band.

In Fig. 3-4, we show an example with parameters $\beta = \gamma = 0.2$, $\alpha_3 = 0.2$, $\Gamma_3 = 0.1$, $\alpha_1 = \Gamma_1 = 0$. In contrary to the preceding example where the lattice is sheared, in this case the lattice is stretched in one direction. Due to the dispersion of the bands, the isofrequency contours are either open or enclose 4 EPs at the same time, making the observation of half-charge polarization winding difficult. As the example given here is fairly similar to the actual band dispersion found in numerical calculations of the band structure near the Γ-point of a square lattice, this highlights the importance of using the correct symmetry breaking operation, matched to the band curvature characteristics, to obtain EPs. In the following, we shall thus mainly focus on lattice shearing symmetry breaking operations. Note that in the hexagonal lattice case,

we wrote down a symmetry breaking term corresponding to α_1; however, due to differences between reciprocal lattice vector definitions (rotated by 45 degrees), the symmetry breaking is in fact more similar to shearing, effectively resulting in behavior as in Fig. 3-3.

3.4 Numerical Simulations of 2D Photonic Crystals

While the analytical model in preceding sections indicates the existence of exceptional points in the perturbative regime, in this section we present numerical simulations of 2D photonic crystals (infinite in the third direction) and demonstrate the existence of polarization contours with half-integer polarization winding.

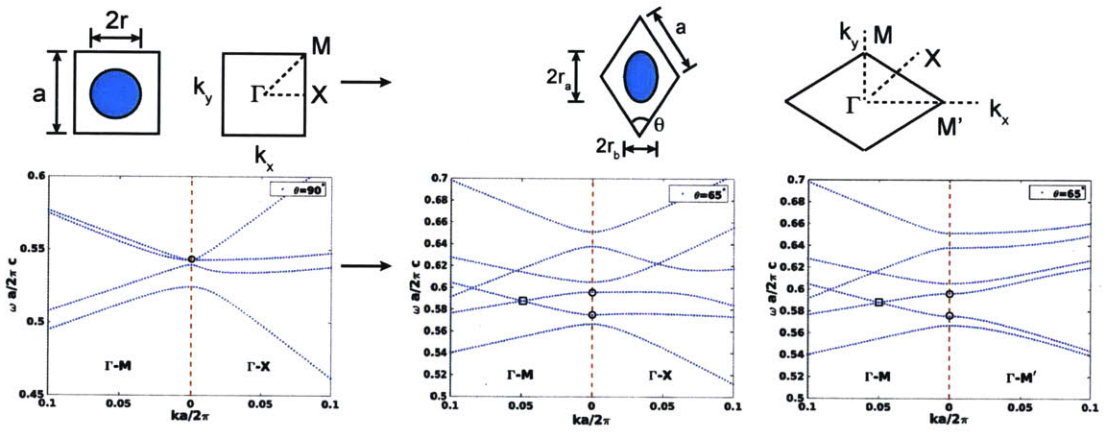

Figure 3-5: Simulation parameters for 2D photonic crystals and line cuts of frequency bands in certain directions. Left: square lattice; Right: sheared lattice with rhombus angle $\theta = 65°$. Circles track the splitting of the quadratic degeneracy, and the rectangle denotes the Dirac point we focus on.

For demonstration purposes, we consider a shearing of the square lattice, as shown in Fig. 3-5. Numerical calculations were performed using the freely available software package MPB [60]. MPB uses preconditioned conjugate-gradient minimization of the block Rayleigh quotient in a planewave basis to determine the eigenmodes of the Maxwell's equations with periodic boundary conditions. By specifying the lattice, structure, and Bloch periodic boundary conditions, we solve the eigenfrequency and

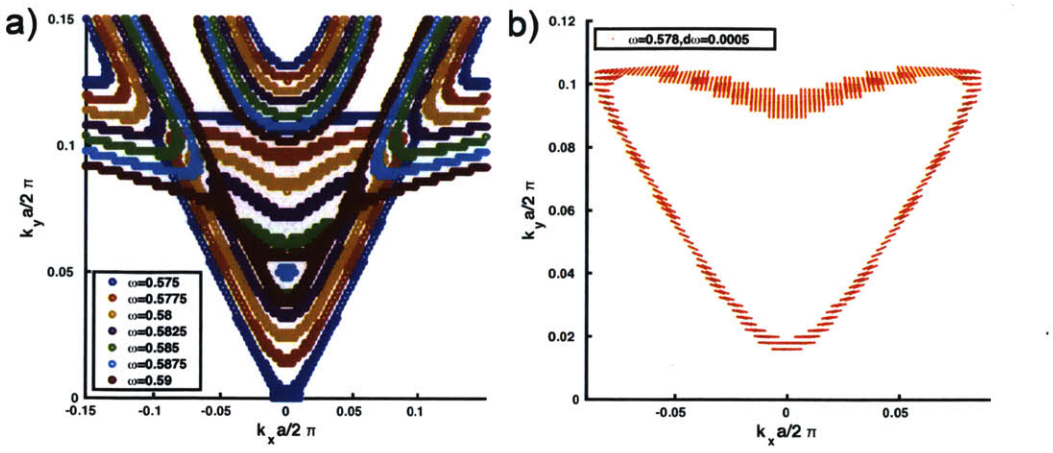

Figure 3-6: (a) Frequency contours for $r/a = 25/84$, $\theta = 65°$, TE polarization. (b) Plot of polarization ellipses at each point along a heart-shaped isofrequency contour, clearly exhibiting a half-integer winding of polarization. Frequencies are in units of $2\pi c/a$.

eigenmodes at each $\vec{k}$-point. From the resulting eigenmodes, we then integrate the Bloch wave function across the Brillouin zone to obtain the polarization vector $\vec{c} = c_x\hat{x} + c_y\hat{y}$, similar to the calculation in the preceding chapter. Note that here we are considering a system with time-reversal symmetry (no loss) as well as C_2^z rotational symmetry and z-mirror symmetry. This guarantees that the Bloch eigenfunctions and $\vec{c}$ can be taken to be real [23].

In these simulations, we use a unit cell with the shape of a rhombus, consisting of a uniform slab material with an elliptical hole etched inside, see top panel of Fig. 3-5 for a schematic. The edge length of the rhombus is defined as a, the radius of the hole when there is no shearing is defined as r, and the angle between two lattice vectors is defined as θ, with $\theta = 90°$ corresponding to the square lattice limit. In the presence of shearing, the holes are deformed from circles into ellipses, and the major axes are chosen to be

$$r_a = 2r\cos^2\frac{\theta}{2}, \quad r_b = 2r\sin^2\frac{\theta}{2}. \tag{3.24}$$

This is consistent with holes resulting from interference lithography, in which two

laser beams are interfered and points where the laser intensity is above a certain threshold are exposed and etched out. By changing the geometric angle between the interfering laser beams, such lattice and hole geometries can be fabricated. For simulations, we normalize all length scales such that $a = 1$. The x and y directions are defined as the symmetry axes of the rhombus. The slab material is assumed to be Si_3N_4 with a refraction index of $n_s = 2.02$, while the hole material is assumed to be index matching liquid with a refraction index of $n_h = 1.462$ (same as SiO_2). The parameters were chosen by optimization over hole radius and angle, to find an example with a relatively wide frequency range where closed isofrequency contours containing a Dirac point can be observed. Such optimization is much faster for 2D simulations than for full 3D slab simulations.

The resulting band structures for TE polarization (electric field is in the $x - y$ plane), $r/a = 25/84$, $\theta = 90°$ or $\theta = 65°$ are shown in Fig. 3-5. When θ is decreased from 90° to 65°, the quadratic degeneracy point splits up and a Dirac point emerges along the Γ-M direction. Note that additional bands are pulled down from the top, and as the angle is tuned a band switching occurred, so that the Dirac point has effectively moved to be between the second and third bands in the figure.

The isofrequency contours around the Dirac point are shown in Fig. 3-6. The width of the contours is chosen to be $d\omega = 0.001 \times 2\pi c/a$, consistent with a quality factor of around 600 in the simulations of photonic crystal slabs below. Below the Dirac point, closed isofrequency contours well-separated from other contours are seen, and they increase in size as one moves away from the Dirac point, until the contour intersects the origin and closes with the symmetric pair of isofrequency contours on the other side. As we increase the frequency above the Dirac point, the contour approaches other frequency bands relatively quickly. Therefore, the range of frequencies over which there is a closed isofrequency contour around the Dirac point is roughly $\omega = (0.577 \sim 0.59) \times 2\pi c/a$. Notice how the contour is similar to the analytical model discussed above, see Fig. 3-3, up to a 45° rotation due to differences in axis definition. This indicates that even out of the perturbative regime, the analytical model can capture many important features of the band structure.

To verify that the isofrequency contour indeed carries half-integer topological charge, we plot polarization ellipses at each point along the isofrequency contour, with the same scale factor at all points, see Fig. 3-6(b). The ellipse is defined by

$$x = x_0 + \Re(c_x e^{i\phi}), y = y_0 + \Re(c_y e^{i\phi}), \phi \in [0, 2\pi), \tag{3.25}$$

where x_0 and y_0 are the center points around which the ellipse is plotted. As discussed above, spatial and time-reversal symmetries of the 2D photonic crystal considered in this section guarantee that the polarization around the isofrequency contour will be linear, as shown in the right panel of Fig. 3-6. As we trace around the contour, the polarization comes back to itself, but with an additional 180° flip, similar to the half charge in Fig. 3-1(d). This can also be seen by noting that the two intersections on the axis have orthogonal orientations. We define the topological charge as [23]

$$q = \frac{1}{2\pi} \oint_C d\vec{k} \cdot \nabla_{\vec{k}} \phi(\vec{k}), \tag{3.26}$$

where $\phi(\vec{k}) = \arg[\vec{v}(\vec{k})]$, $\vec{v}(\vec{k})$ being the major axis of the polarization ellipse [39, 61], which in this case is the direction of linear polarization. By inspection, we see that our contour has a topological charge of $q = -1/2$, corresponding to a Mobius strip.

In general, two bands that belong to the same TE/TM polarization but have a symmetry mismatch along high symmetry lines can often give rise to half-integer polarization winding. If these two bands meet along the high symmetry line, the symmetry mismatch prohibits them from interacting along this line, so the two bands will cross each other. On the other hand, away from the high symmetry line, the coupling between the bands will open up a gap, similar to the well-known avoided crossing. We are therefore generically left with a Dirac point on the high symmetry line, and on the two sides of the Dirac point along the high symmetry line, the modes will have different polarization configurations, hence giving rise to a half-integer topological charge.

3.5 Numerical Simulations of Photonic Crystal Slabs

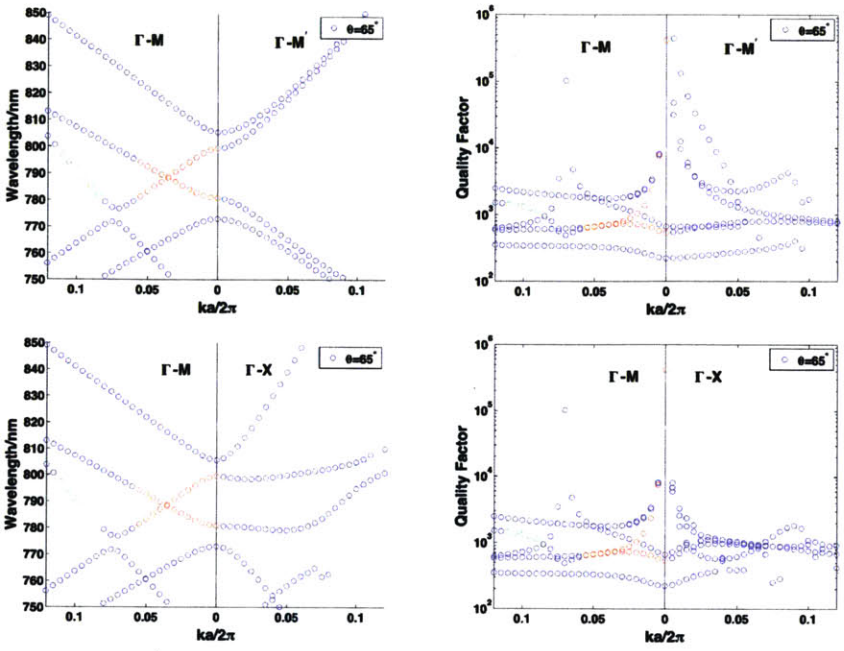

Figure 3-7: TE band structure and quality factor for $a = 530$ nm, $r = 157$ nm, $t = 180$ nm, $\theta = 65°$. The range of frequencies and bands that we focus on are marked in red, and the bands used for excitation are marked in green. Note that the green bands have a quality factor of around 1000 around the wavelength of interest.

In this section, we present simulation results of photonic crystal slabs to verify the existence of exceptional points and half-integer charge polarization winding along isofrequency contours.

Due to the degeneracy between eigenvalues near the exceptional point, the approach in the preceding chapter of first performing an FDTD simulation and then using Fourier transforms to determine the appropriate eigenmodes does not work well in this system. Therefore, we determine the eigenmodes using frequency domain finite element method simulations with the commercial software package COMSOL Multiphysics [62]. We use similar parameters as in the preceding section, except that there is now an additional variable describing the thickness of the slab t, and perfectly matched layers (PML) are placed on the top and bottom to absorb outgoing waves. Polarization vectors are extracted by integrating the Bloch wave functions on a plane

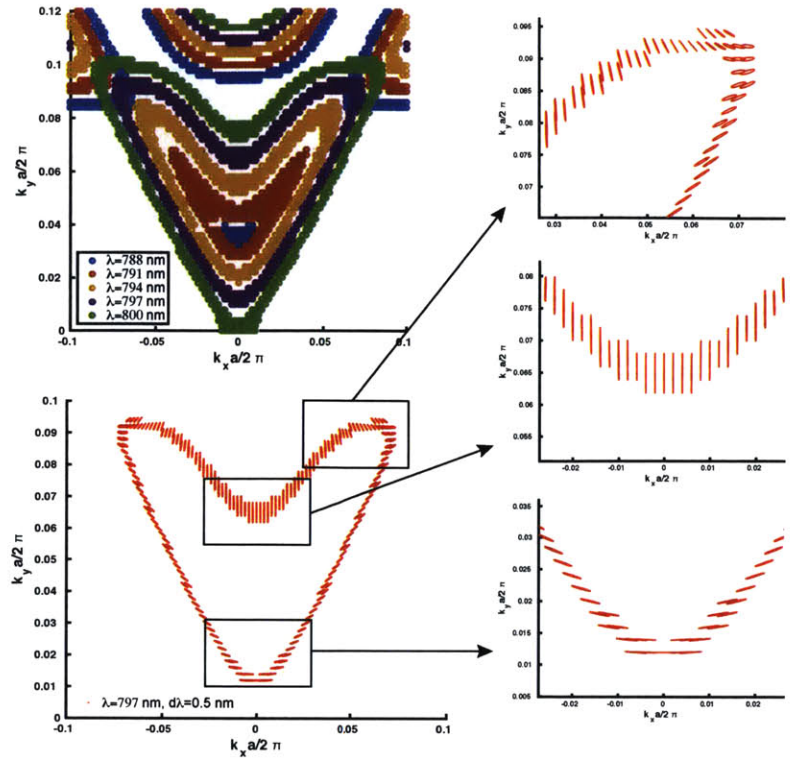

Figure 3-8: Isofrequency contours and polarization ellipses for the photonic crystal slab. Top left: isofrequency contours of width 1 nm, clearly forming closed loops; Bottom left: polarization ellipses along the specific contour with wavelength 797 nm; Right: zoom in on different parts of the polarization ellipses. The polarization is mostly linear, except close to the upper left and upper right corners of the heart shape.

that is between the slab and PML.

The simulation parameters are rhombus side length $a = 530$ nm, hole radius without shearing $r = 157$ nm, slab thickness $t = 180$ nm, rhombus angle $\theta = 65°$, slab refraction index $n_s = 2.02$, substrate, superstrate and hole refraction index $n_h = 1.462$. As in the previous section, we consider the TE-like polarization [1]. The band structure and quality factors along certain line cuts are shown in Fig. 3-7. The pair of bands we use to form the closed isofrequency contours are labeled in red, while the band to be used for excitation and pumping, as discussed in more detail in the next section, is labeled in green.

The radiation loss in a slab of finite thickness breaks the time-reversal symmetry of

the system. Therefore, contrary to the preceding section, c_x and c_y will now in general be complex vectors, and the polarization at each point will be an ellipse when c_x, c_y are out of phase. The topological charge along the polarization contour, however, can still be defined through Eqs. (3.25,3.26) by examining the major axis of the ellipse.

The isofrequency contours around the exceptional points are shown in Fig. 3-8. We see the formation of closed isofrequency contours containing a single pair of exceptional points for a range of wavelengths from 788 nm up to 800 nm. Along an isofrequency contour, the field is mostly linearly polarized, and exhibits a Mobius polarization winding with topological charge $q = -1/2$.

To verify the existence of exceptional points in the band structure, we traverse loops in momentum space and trace the eigenvalues along these loops. As discussed in section 3.2.4, if a single EP is enclosed, the eigenvalues will switch places with each other, while if there are no EPs, the eigenvalues will return to themselves. In Fig. 3-9, we plot examples of two such contours, one enclosing an EP and the other not. The observed eigenvalue switching behavior verifies the existence of EPs. By systematically changing the loop, we find that an EP is located around $(k_{x0}, k_{y0}) = (0.036, 0.001) \times 2\pi/a$. The other 3 EPs will be located at $(\pm k_{x0}, \pm k_{y0})$ by symmetry.

The main features of the photonic crystal slab results are again consistent with the analytical model and 2D photonic crystal simulations, confirming our theory and numerical calculations.

3.6 Experimental Feasibility

The designs above should be readily fabricated in large area photonic crystal slabs. The parameters we have used are achievable with current interference lithography setups. The in-plane periodicity required for the laser is 480 nm, which is achievable by tilting the 355 nm laser beam used for interference. The refraction index of a Si_3N_4 slab and SiO_2 substrate are already matched with our simulations, and the refraction indices in the holes and superstrate can be tuned to the design value of 1.462 by using index matching liquid [57]. Moreover, fine tuning to compensate for fabrication

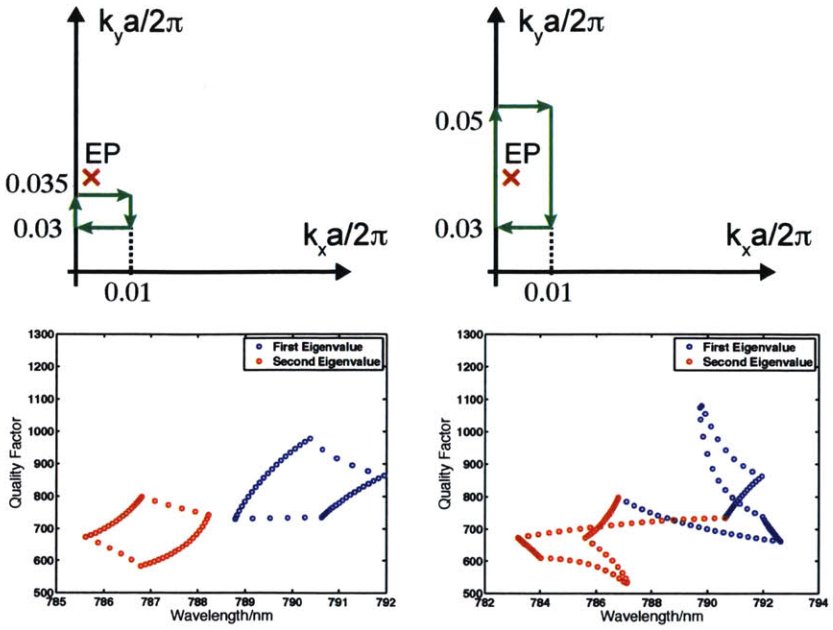

Figure 3-9: Loops in momentum space verifying the existence of exceptional points. Left: the eigenvalues return to themselves when the loop doesn't enclose an EP; Right: when the loop contains an exceptional point, the eigenvalues switch.

disorder can be achieved with index tuning. Using interference lithography and tuning the tilting angle of the interfering laser beams as well as the in-plane angle between the laser beams, it should be possible to produce differences in the lattice vector lengths and shear the lattice, thereby generating nonzero α_1 and α_3. On the other hand, other types of symmetry breaking corresponding to α_2 might be more difficult to implement. An alternative, somewhat more complicated method to fabricate a roughly hexagonal lattice structure to explore other band structures would be to use three beams to interfere and produce more complicated shapes of holes or rods.

Direct imaging of the polarization features on the isofrequency contours can be achieved using resonant-enhanced scattering from natural fabrication disorder [63]. This experimental scheme excites a resonance at the same frequency as the target isofrequency contour but with a different momentum. Disorder and roughness introduced during the fabrication process scatter light in this resonance to the resonance of interest, so that light is emitted from the slab in directions corresponding to isofre-

quency contours of the desired bands. By placing a polarizer and/or waveplate in the far field, we can directly image the polarization at each point on this isofrequency contour. By mapping out the polarization states on the entire isofrequency contour, we can verify that the scattered light indeed forms a half-integer topological charge. The scattered light intensity can be computed from temporal coupled-mode theory to be [63]

$$\frac{P_{scat}}{P_{in}} = \frac{2\gamma_r\gamma_{scat}}{(\omega-\omega_0)^2+(\gamma_r+\gamma_{scat}+\gamma_0)^2}, \tag{3.27}$$

where P_{scat} is the scattered power, P_{in} is the incoming power, γ_r the radiative decay rate of the excitation resonance, γ_{scat} the scattering decay rate between resonances, γ_0 absorption decay rate (often negligible), ω is the excitation frequency and ω_0 is the resonance frequency. This quantity is maximized on-resonance with frequency bands and when the impedance matching condition $\gamma_r = \gamma_{scat}$ is satisfied.

To perform measurements of the polarization Mobius strip, we require the following experimental conditions:

1. There are closed isofrequency contours encircling two exceptional points.

2. The excitation light source frequency can be tuned across the range of closed isofrequency contours that contain the exceptional points, with a linewidth that is preferably less than the width corresponding to the quality factor of the bands.

3. The width of the bands combined with the far-field angular resolution is such that individual frequency contours can be separated and resolved, and the polarization can be mapped out along the frequency contour. Other bands in the same region are either non-intersecting or very weak.

4. There exist other bands with the same frequency but at other wavevectors, such that the radiative quality factor of this band is matched to the scattering quality factor (see above). This allows light to be efficiently coupled into resonances in the photonic crystal slab and scattered into the desired contour.

In addition, the following characteristics are also desirable but not strictly required:

5. Isofrequency contour has a more circular shape. This might be useful if the light emitted from the photonic crystal is used for other applications, such as manipulation of particles or fabricating exotic shapes. Alternatively, beam shaping afterwards could produce more favorable contours.

6. Along the isofrequency contour, the polarization is as close to linearly polarized as possible. This will help to eliminate the ambiguity of ellipse axes associated with circular polarization.

In our simulations above, we have demonstrated the existence of isofrequency contours enclosing exceptional points. The wavelength around which the effect is observable has been engineered to be around 795 nm, lying well in the frequency range over which Ti:Sapphire lasers can be tuned (650 nm-1100 nm), and where the laser has linewidths less than 1 nm.

The quality factor of the bands of interest is around 600, see Fig. 3-7, corresponding to a wavelength width of roughly 1 nm. From Fig. 3-8 with band widths of 1 nm, we see that the isofrequency contours are well separated and the polarization can be easily differentiated along the contour. The angle of emission is a few degrees, so the contour should be easily observable. There exist additional TM-polarized bands in the same region, but due to the mirror symmetry in the z-direction, exciting resonances in TE bands will not scatter very strongly into TM bands (this has been experimentally verified in Ref. [63]).

We use the bands located around $k_y = 0.1 \times 2\pi/a$ at $\lambda = 790$ nm to couple light into the resonance. These have a total quality factor of 1000, or a single-sided coupling quality factor of 2000, well matched to the scattering quality factor in typical samples fabricated by interference lithography. It should therefore be possible to efficiently couple light into the resonances.

Due to the parameter choice the isofrequency contour is not very round (but still very pretty!); further optimization could be performed to produce a more favorable

shape. Along most points on the isofrequency contour in our example, the polarization is roughly linear, so that the topological charge is well-defined.

Therefore, all requirements for observing half-integer topological charges are satisfied with the photonic crystal slab we have designed, and experiments should be able to verify the generation of isofrequency contours with Mobius strip polarization from these structures.

Chapter 4

Conclusion and Future Outlook

In this thesis we have discussed some interesting possibilities of tailoring light emission from photonic crystal slabs. In particular, we have focused on two important properties to pursue with these structures, one of directionality and controlled emission, and the other of exploiting topological features of the band structure.

In chapter 2, we derived a temporal coupled-mode theory formalism to analytically calculate the scattering matrix from a photonic crystal slab of arbitrary geometry and at arbitrary incident angle. The reflection and transmission spectrum is calculated under this framework and bounds on the achievable coupling asymmetry are derived. The bounds are verified with numerical simulations of photonic crystal structures, and we showed how these bounds can be saturated by parameter optimization. We then focus on the particular example of an inversion-symmetric structure and give examples of both highly asymmetric coupling and rapid switching of coupling direction.

It will be interesting to extend our temporal coupled-mode theory formalism further to include non-linear effects (perturbation theory), gain and loss (additional ports corresponding to gain or loss channels), different substrates and superstrates (modified direct pathway matrix), and time-reversal symmetry breaking structures (magneto-optical effects could potentially be incorporated by choosing an appropriate basis [64]). Including such effects into the formalism may allow us to examine fundamental bounds on asymmetric emission in more complicated systems, and explore novel effects on the Fano resonance and transmission spectrum.

In chapter 3, we show the possibility of generating Mobius strips of polarization from photonic crystal slabs. From a simple two-band model constrained by symmetry considerations, we examine the band structure in different parameter regimes for a square lattice and hexagonal lattice, and find that exceptional points with nontrivial topological characteristics arise in these systems. We then demonstrate using numerical calculations of the band structure and polarization on isofrequency contours that half-integer vector beams can be generated from photonic crystal slabs. Systematic optimization of the parameters to maximize the range of frequencies over which this effect is observable will make experimental demonstrations easier.

In the future, it would be interesting to engineer the band structures such that the isofrequency contours are more isotropic in shape. Another possibility is to generate higher order vector beams with half-integer polarization winding. From a physics viewpoint, exploring other types of band structures and the effect of adding radiation loss will allow new topological features to be extracted and understood. Potential candidates may include higher order exceptional points, double Dirac cones [65, 66], flat bands in Lieb lattices or Kagome lattices [67, 68], and other nontrivial band topologies. An alternative direction would be to combine the possibility of engineering asymmetric emission and generating nontrivial polarization topologies, such that the photonic crystal slab radiates with one topological configuration on one side and a different one on the other side. We hope that our work is only the tip of an iceberg to the wealth of phenomena in photonic structures that will reveal interesting new physics and important applications.

Appendix A

Extended Results from Analytical Model

In this appendix, we give some additional examples of the possible isofrequency contours and exceptional point layouts based on the analytical model. Without loss of generality, we may choose $\beta, \gamma > 0$, since negative values can be obtained by appropriate choices of the symmetry breaking terms and switching the bands. In the following figures, we shall show 3D plots of the frequencies, as well as 2D plots of the decay rates and isofrequency contours, all as a function of the in-plane momentum. From Eq. (3.4), the imaginary part of the eigenvalue (corresponding to the decay rate) will always appear in conjugate pairs with the same magnitude, so we only plot one of them. In the case where the two isofrequency contours are qualitatively similar, we only show one of them. Due to the quadratic dispersion of the bands, the spacing of isofrequencies is much closer at higher momenta, so we choose nonuniform frequency spacings instead to illustrate the main features of the contours.

In the case where there is no symmetry breaking term, the eigenvalues are given by

$$E(k_x, k_y) = \gamma(k_x^2 + k_y^2) \pm \sqrt{(k_x^2 + k_y^2)^2 + (\beta^2 - 1)(k_x^2 - k_y^2)^2}, \tag{A.1}$$

so that along the k_x, k_y axis the dispersion is $E \sim (\gamma \pm |\beta|)k^2$ and along the $k_x = \pm k_y$

axis the dispersion is $E \sim (\gamma \pm 1)k^2$. Therefore, the parameters γ and β act to control the curvature of the band in different directions.

A.1 Case I: $\beta = 1$

We start with $\beta = 1$, corresponding to the fixed value for the hexagonal lattice and also achievable for the square lattice. Plugging this into the expression for the eigenvalues Eq. (3.4), the terms can be rearranged as only a function of k^2, so this is a case where the bands are isotropic in different directions prior to symmetry breaking. The isofrequency contours before symmetry breaking will simply be circles.

For simplicity, first consider $\gamma = 0$, where according to Eq. (3.4), the top and bottom bands will have the same shape but curve in opposite directions.

When $\alpha_3 \neq 0$ (stretching), $\alpha_1 = 0$, the σ_1 and σ_2 reflection symmetries of the square lattice are preserved, so the EPs are seen to appear in the horizontal or vertical directions depending on the sign of α_3. This is illustrated in Fig. A-1. Increasing α_3 increases the distance from the origin to the EPs, while increasing Γ_3 increases the distance between the EPs where they split along a hyperbola. The effect of α_1 is similar due to the isotropic nature of the original bands, except the direction of the EPs is rotated by 45 degrees. When both α_1, α_3 are nonzero, the directions of the EPs will be distorted, but the general shape of the contours are fairly similar to Fig. A-1(b).

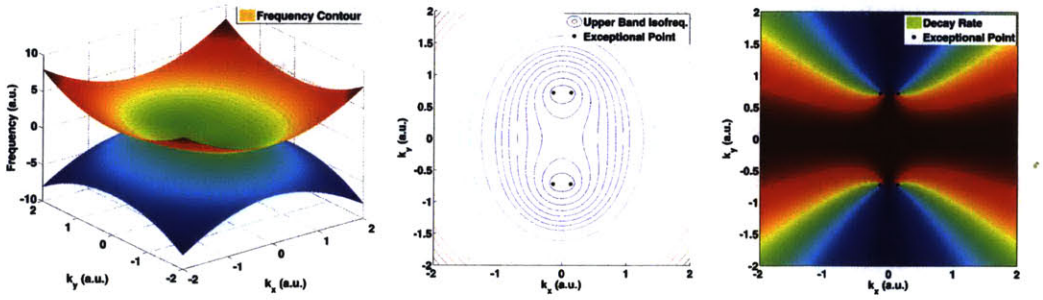

Figure A-1: Frequency spectrum, isofrequency contours and decay rates for parameter choice $\beta = 1$, $\gamma = \alpha_1 = \Gamma_1 = 0$, $\alpha_3 = 0.5$, $\Gamma_3 = 0.2$ in the analytical model.

Now we move on to examples where $\beta = 1$, but $\gamma \neq 0$. First consider $\gamma < \beta$, with $\gamma = 0.8$ as an example. In this case, one of the bands will be flatter than the other, giving rise to differences in the isofrequency contours. In the example in Fig. A-2, the upper band no longer has a wide range of isofrequency contours that enclose only 2 EPs, and instead the contours encircle all 4 EPs, while the lower band still has many isofrequency contours containing 2 EPs.

For $\gamma > \beta$, the two bands bend up in the same direction, as in Fig. A-3. On both bands, most isofrequency contours will now contain all 4 EPs simultaneously, so the emitted light will not have a polarization Mobius strip configuration. Note here however that for larger values of loss differences between bands, on the lower bands and close to the EP, there are a narrow range of isofrequency contours that only contain one EP. Further work is required to see if this can appear in realistic band structures, and if they are of any significance.

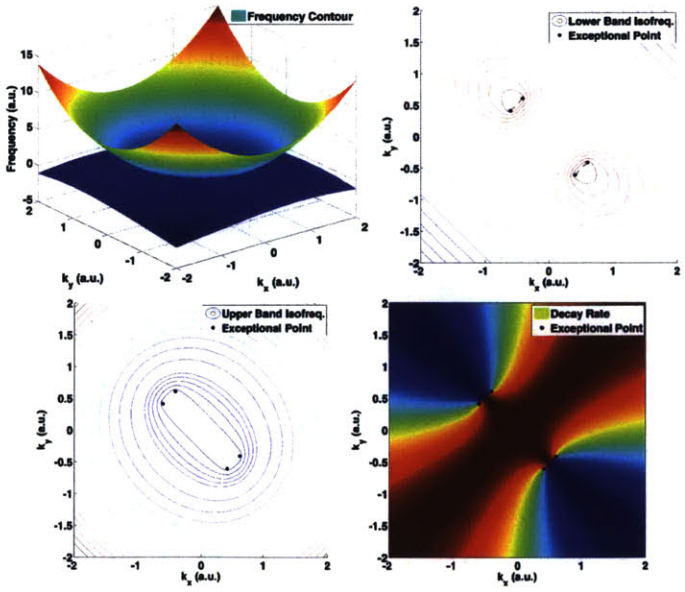

Figure A-2: Frequency spectrum, isofrequency contours and decay rates for parameter choice $\beta = 1$, $\gamma = 0.8$, $\alpha_1 = 0.5$, $\Gamma_1 = 0.2$, $\alpha_3 = \Gamma_3 = 0$ in the analytical model.

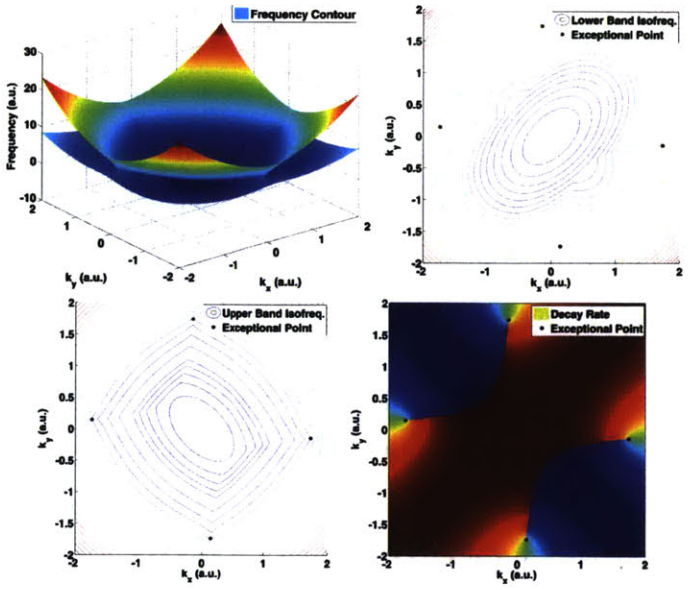

Figure A-3: Frequency spectrum, isofrequency contours and decay rates for parameter choice $\beta = 1$, $\gamma = 2$, $\alpha_1 = 0.5$, $\Gamma_1 = 3$, $\alpha_3 = \Gamma_3 = 0$ in the analytical model.

A.2 Case II: $\beta = 0.2$

Here we consider the case where the control parameter β is small, and choose the specific value of $\beta = 0.2$ for our calculations. This case corresponds to when the difference between band curvature along the k_x, k_y axis is smaller. In the main text, due to the relevance of such a structure to calculated 2D photonic band structures, we have already presented some results for $\beta = \gamma = 0.2$, see Fig. 3-3 and Fig. 3-4.

For $\gamma = 0$, symmetry breaking forms closed contours as in the previous section. The main difference here is that due to the anisotropy of bands in different directions, α_1 and α_3 symmetry breaking terms now have different effects, as seen in Fig. A-4. The resulting isofrequency contours are more circular in the case of stretching, while they are closer to hyperbolas in the case of shearing. However, both contain closed isofrequency contours.

For small but finite γ, with $\gamma = 0.2$ as an example, the bands will be flat along the $k_x = 0$ and $k_y = 0$ axes before symmetry breaking. This results in one of the directions having open contours after symmetry breaking, as seen in Fig. 3-3 and

Fig. 3-4. When the imaginary part of the symmetry breaking term is greater, shown in Fig. A-5, we again see pockets of isofrequency contours that only contain a single EP, and closed isofrequency contours that are near the EPs but do not contain them.

When γ is large, we return to a similar case as when γ is greater than 1 in the previous section, in which both bands bend in the same direction, and the isofrequency contours contain all 4 EPs at the same time.

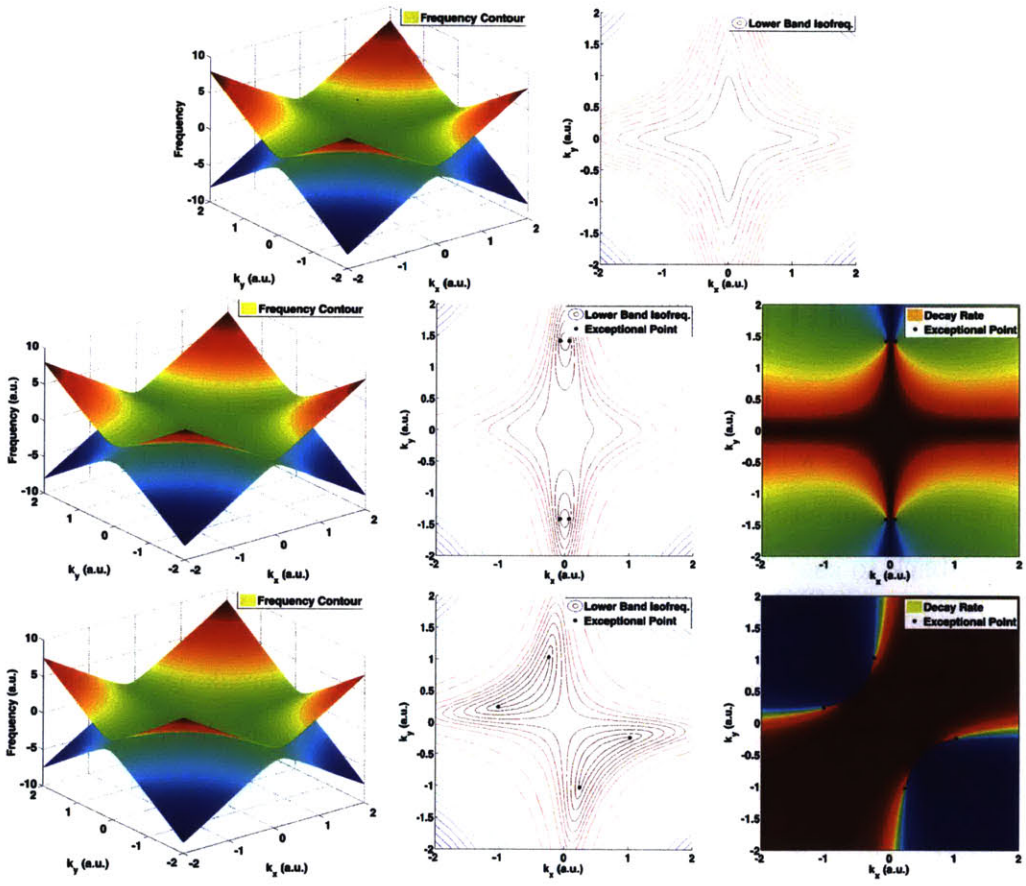

Figure A-4: Frequency spectrum, isofrequency contours and decay rates for parameter choice top: $\beta = 0.2$, $\gamma = 0$, $\alpha_1 = \Gamma_1 = \alpha_3 = \Gamma_3 = 0$, middle: $\beta = 0.2$, $\gamma = 0$, $\alpha_1 = 0.4$, $\Gamma_1 = 0.2$, $\alpha_3 = \Gamma_3 = 0$, bottom: $\beta = 0.2$, $\gamma = 0$, $\alpha_3 = 0.5$, $\Gamma_3 = 0.2$, $\alpha_1 = \Gamma_1 = 0$ in the analytical model.

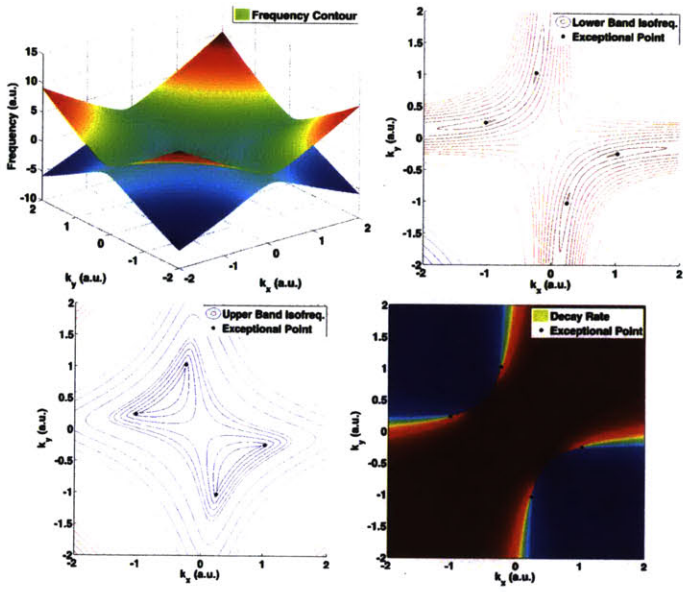

Figure A-5: Frequency spectrum, isofrequency contours for parameter choice $\beta = 0.2$, $\gamma = 0.2$, $\alpha_1 = 0.5$, $\Gamma_1 = 0.2$, $\alpha_3 = \Gamma_3 = 0$ in the analytical model.

A.3 Case III: $\beta = 5$

Here we consider the case where β is relatively large. We choose $\beta = 5$; the difference in band curvatures will thus be smaller along the $k_y = \pm k_x$ axis. Most of the qualitative features can already be understood by a 45 degree rotation of the axes, which brings us back to case II.

The example we provide here in Fig. A-6 is when both β and γ are large. One direction on the lower band will be flat prior to symmetry breaking, giving rise to open frequency contours in diagonal directions. The other contains closed contours of all 4 EPs, and there are isofrequency contours closer to the Γ point than the EPs.

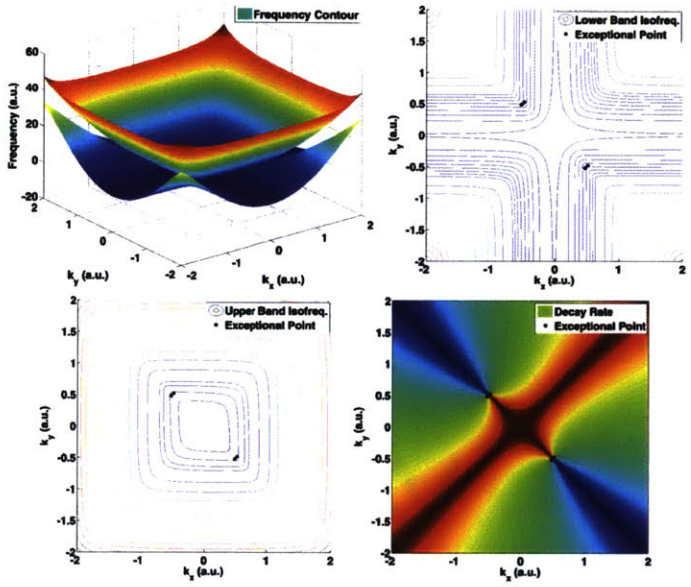

Figure A-6: Frequency spectrum, isofrequency contours and decay rates for parameter choice $\beta = 5$, $\gamma = 5$, $\alpha_1 = 0.5$, $\Gamma_1 = 0.2$, $\alpha_3 = \Gamma_3 = 0$ in the analytical model.

Bibliography

[1] J. D. Joannopoulos, S. G. Johnson, J. N. Winn, and R. D. Meade. *Photonic Crystals: Molding the Flow of Light (Second Edition).* Princeton University Press, 2011.

[2] E. Yablonovitch. Inhibited Spontaneous Emission in Solid-State Physics and Electronics. *Physical Review Letters*, 58(20):2059–2062, may 1987.

[3] M. Soljačić, S. G. Johnson, S. Fan, M. Ibanescu, E. Ippen, and J. D. Joannopoulos. Photonic-crystal slow-light enhancement of nonlinear phase sensitivity. *Journal of the Optical Society of America B*, 19(9):2052, sep 2002.

[4] Q. Zhan. Cylindrical vector beams: from mathematical concepts to applications. *Advances in Optics and Photonics*, 1(1):1, jan 2009.

[5] J. Lee, B. Zhen, S.-L. Chua, O. Shapira, and M. Soljačić. Fabricating centimeter-scale high quality factor two-dimensional periodic photonic crystal slabs. *Optics express*, 22(3):3724–31, feb 2014.

[6] J. Lee, B. Zhen, S.-L. Chua, W. Qiu, J. D. Joannopoulos, M. Soljačić, and O. Shapira. Observation and differentiation of unique high-Q optical resonances near zero wave vector in macroscopic photonic crystal slabs. *Physical review letters*, 109(6):067401, aug 2012.

[7] S. Fan and J. D. Joannopoulos. Analysis of guided resonances in photonic crystal slabs. *Physical Review B*, 65(23):235112, jun 2002.

[8] K. Hirose, Y. Liang, Y. Kurosaka, A. Watanabe, T. Sugiyama, and S. Noda. Watt-class high-power, high-beam-quality photonic-crystal lasers. *Nature Photonics*, 8(5):406–411, apr 2014.

[9] D. Taillaert, P. Bienstman, and R. Baets. Compact efficient broadband grating coupler for silicon-on-insulator waveguides. *Optics Letters*, 29(23):2749, dec 2004.

[10] R. L. Roncone, L. Li, K. A. Bates, J. J. Burke, L. Weisenbach, and B. J. Zelinski. Design and fabrication of a single leakage-channel grating coupler. *Applied optics*, 32(24):4522–8, aug 1993.

[11] D. Vermeulen, S. Selvaraja, P. Verheyen, G. Lepage, W. Bogaerts, P. Absil, D. Van Thourhout, and G. Roelkens. High-efficiency fiber-to-chip grating couplers realized using an advanced CMOS-compatible silicon-on-insulator platform. *Optics express*, 18(17):18278–83, aug 2010.

[12] M. Fan, M. Popović, and F. X. Kartner. High Directivity, Vertical Fiber-to-Chip Coupler with Anisotropically Radiating Grating Teeth. In *2007 Conference on Lasers and Electro-Optics (CLEO)*, pages 1–2, may 2007.

[13] Y. Ota, S. Iwamoto, and Y. Arakawa. Asymmetric out-of-plane power distribution in a two-dimensional photonic crystal nanocavity. *Optics letters*, 40(14):3372–5, jul 2015.

[14] K. X. Wang, Z. Yu, S. Sandhu, and S. Fan. Fundamental bounds on decay rates in asymmetric single-mode optical resonators. *Optics letters*, 38(2):100–2, jan 2013.

[15] W. Suh, Z. Wang, and S. Fan. Temporal coupled-mode theory and the presence of non-orthogonal modes in lossless multimode cavities. *IEEE Journal of Quantum Electronics*, 40(10):1511–1518, oct 2004.

[16] S. Fan, W. Suh, and J. D. Joannopoulos. Temporal coupled-mode theory for the Fano resonance in optical resonators. *Journal of the Optical Society of America A*, 20(3):569, mar 2003.

[17] M. G. Moharam and T. K. Gaylord. Rigorous coupled-wave analysis of planar-grating diffraction. *Journal of the Optical Society of America*, 71(7):811, jul 1981.

[18] V. Liu and S. Fan. S4 : A free electromagnetic solver for layered periodic structures. *Computer Physics Communications*, 183(10):2233–2244, oct 2012.

[19] E. Hecht. *Optics*. Addison-Wesley, 2001.

[20] A. Taflove, A. Oskoòi, and S. G. Johnson. *Advances in FDTD Computational Electrodynamics: Photonics and Nanotechnology*. Artech House, 2013.

[21] A. F. Oskooi, D. Roundy, M. Ibanescu, P. Bermel, J. D. Joannopoulos, and S. G. Johnson. Meep: A flexible free-software package for electromagnetic simulations by the FDTD method. *Computer Physics Communications*, 181(3):687–702, mar 2010.

[22] V. A. Mandelshtam and H. S. Taylor. Harmonic inversion of time signals and its applications. *The Journal of Chemical Physics*, 107(17):6756, 1997.

[23] B. Zhen, C. W. Hsu, L. Lu, A. D. Stone, and M. Soljačić. Topological Nature of Optical Bound States in the Continuum. *Physical Review Letters*, 113(25):257401, dec 2014.

[24] A. Yaacobi, J. Sun, M. Moresco, G. Leake, D. Coolbaugh, and M. R. Watts. Integrated phased array for wide-angle beam steering. *Optics letters*, 39(15):4575–8, aug 2014.

[25] C. W. Hsu, B. Zhen, S.-L. Chua, S. G. Johnson, J. D. Joannopoulos, and M. Soljačić. Bloch surface eigenstates within the radiation continuum. *Light: Science & Applications*, 2(7):e84, jul 2013.

[26] C. W. Hsu, B. Zhen, J. Lee, S.-L. Chua, S. G. Johnson, J. D. Joannopoulos, and M. Soljačić. Observation of trapped light within the radiation continuum. *Nature*, 499(7457):188–91, jul 2013.

[27] S. Y. Chou, P. R. Krauss, and P. J. Renstrom. Imprint Lithography with 25-Nanometer Resolution. *Science*, 272(5258):85–87, apr 1996.

[28] J. Schrauwen, F. V. Laere, D. V. Thourhout, and R. Baets. Focused-Ion-Beam Fabrication of Slanted Grating Couplers in Silicon-on-Insulator Waveguides. *IEEE Photonics Technology Letters*, 19(11):816–818, jun 2007.

[29] M. J. Burek, N. P. de Leon, B. J. Shields, B. J. M. Hausmann, Y. Chu, Q. Quan, A. S. Zibrov, H. Park, M. D. Lukin, and M. Lončar. Free-standing mechanical and photonic nanostructures in single-crystal diamond. *Nano letters*, 12(12):6084–9, dec 2012.

[30] Y. Kurosaka, S. Iwahashi, Y. Liang, K. Sakai, E. Miyai, W. Kunishi, D. Ohnishi, and S. Noda. On-chip beam-steering photonic-crystal lasers. *Nature Photonics*, 4(7):447–450, may 2010.

[31] L. Allen, M. W. Beijersbergen, R. J. C. Spreeuw, and J. P. Woerdman. Orbital angular momentum of light and the transformation of Laguerre-Gaussian laser modes. *Physical Review A*, 45(11):8185–8189, jun 1992.

[32] S. Franke-Arnold, L. Allen, and M. J. Padgett. Advances in optical angular momentum. *Laser & Photonics Review*, 2(4):299–313, aug 2008.

[33] H. He, M. E. Friese, N. R. Heckenberg, and H. Rubinsztein-Dunlop. Direct observation of transfer of angular momentum to absorptive particles from a laser beam with a phase singularity. *Physical review letters*, 75(5):826–829, jul 1995.

[34] K. Bongs, S. Burger, S. Dettmer, D. Hellweg, J. Arlt, W. Ertmer, and K. Sengstock. Waveguide for Bose-Einstein condensates. *Physical Review A*, 63(3):031602, feb 2001.

[35] A. Vaziri, G. Weihs, and A. Zeilinger. Experimental two-photon, three-dimensional entanglement for quantum communication. *Physical review letters*, 89(24):240401, dec 2002.

[36] R. Dorn, S. Quabis, and G. Leuchs. Sharper focus for a radially polarized light beam. *Physical review letters*, 91(23):233901, dec 2003.

[37] V. G. Niziev and A. V. Nesterov. Influence of beam polarization on laser cutting efficiency. *Journal of Physics D: Applied Physics*, 32(13):1455–1461, jul 1999.

[38] I. Freund. Cones, spirals, and Möbius strips, in elliptically polarized light. *Optics Communications*, 249(1-3):7–22, may 2005.

[39] T. Bauer, P. Banzer, E. Karimi, S. Orlov, A. Rubano, L. Marrucci, E. Santamato, R. W. Boyd, and G. Leuchs. Observation of optical polarization Möbius strips. *Science*, 347(6225):964–6, feb 2015.

[40] D. Pohl. Operation of a Ruby Laser in the Purely Transverse Electric Mode TE01. *Applied Physics Letters*, 20(7):266, oct 1972.

[41] M. Stalder and M. Schadt. Linearly polarized light with axial symmetry generated by liquid-crystal polarization converters. *Optics Letters*, 21(23):1948, dec 1996.

[42] Z. Bomzon, G. Biener, V. Kleiner, and E. Hasman. Radially and azimuthally polarized beams generated by space-variant dielectric subwavelength gratings. *Optics Letters*, 27(5):285, mar 2002.

[43] N. Radwell, R. D. Hawley, J. B. Götte, and S. Franke-Arnold. Achromatic vector vortex beams from a glass cone. *Nature communications*, 7:10564, jan 2016.

[44] L. Lu, J. D. Joannopoulos, and M. Soljačić. Topological photonics. *Nature Photonics*, 8(11):821–829, oct 2014.

[45] C. E. Rüter, K. G. Makris, R. El-Ganainy, D. N. Christodoulides, M. Segev, and D. Kip. Observation of parity-time symmetry in optics. *Nature Physics*, 6(3):192–195, jan 2010.

[46] H. Cao and J. Wiersig. Dielectric microcavities: Model systems for wave chaos and non-Hermitian physics. *Reviews of Modern Physics*, 87(1):61–111, jan 2015.

[47] Y. D. Chong, X.-G. Wen, and M. Soljačić. Effective theory of quadratic degeneracies. *Physical Review B*, 77(23):235125, jun 2008.

[48] T. Kato. *Perturbation Theory for Linear Operators*. Springer Science & Business Media, 2012.

[49] W. D. Heiss. Repulsion of resonance states and exceptional points. *Physical Review E*, 61(1):929–932, jan 2000.

[50] T. Inui, Y. Tanabe, and Y. Onodera. *Group Theory and Its Applications in Physics*, volume 78 of *Springer Series in Solid-State Sciences*. Springer Berlin Heidelberg, Berlin, Heidelberg, 1990.

[51] K. Sakoda. *Optical Properties of Photonic Crystals*, volume 15. Springer, 2005.

[52] S. Raghu and F. D. M. Haldane. Analogs of quantum-Hall-effect edge states in photonic crystals. *Physical Review A*, 78(3):033834, sep 2008.

[53] N. Moiseyev. *Non-Hermitian Quantum Mechanics*. Cambridge University Press, 2011.

[54] C. Dembowski, H. Gräf, H. L. Harney, A. Heine, W. D. Heiss, H. Rehfeld, and A. Richter. Experimental observation of the topological structure of exceptional points. *Physical review letters*, 86(5):787–90, jan 2001.

[55] W. D. Heiss. The physics of exceptional points. *Journal of Physics A: Mathematical and Theoretical*, 45(44):444016, nov 2012.

[56] I. Freund. Multitwist optical Möbius strips. *Optics letters*, 35(2):148–50, jan 2010.

[57] B. Zhen, C. W. Hsu, Y. Igarashi, L. Lu, I. Kaminer, A. Pick, S.-L. Chua, J. D. Joannopoulos, and M. Soljačić. Spawning rings of exceptional points out of Dirac cones. *Nature*, advance on, sep 2015.

[58] J. Mei, Y. Wu, C. T. Chan, and Z.-Q. Zhang. First-principles study of Dirac and Dirac-like cones in phononic and photonic crystals. *Physical Review B*, 86(3):035141, jul 2012.

[59] A. Fang, Z. Q. Zhang, S. G. Louie, and C. T. Chan. Klein tunneling and supercollimation of pseudospin-1 electromagnetic waves. *Physical Review B*, 93(3):035422, jan 2016.

[60] S. G. Johnson and J. D. Joannopoulos. Block-iterative frequency-domain methods for Maxwell's equations in a planewave basis. *Optics Express*, 8(3):173, jan 2001.

[61] I. Freund. Optical Möbius strips, twisted ribbons, and the index theorem. *Optics letters*, 36(23):4506–8, dec 2011.

[62] Comsol multiphysics 4.4. `http://www.comsol.com`.

[63] E. C. Regan, Y. Igarashi, B. Zhen, I. Kaminer, C. W. Hsu, Y. Shen, J. D. Joannopoulos, and M. Soljačić. Coherent Photon Scattering and Direct Imaging of the Iso-frequency Contours in Large-area Photonic Crystal Slabs. *arxiv:1512.04147*, dec 2015.

[64] Z. Wang and S. Fan. Magneto-optical defects in two-dimensional photonic crystals. *Applied Physics B*, 81(2-3):369–375, jul 2005.

[65] K. Sakoda. Double Dirac cones in triangular-lattice metamaterials. *Optics express*, 20(9):9925–39, apr 2012.

[66] K. Sakoda. Dirac cone in two- and three-dimensional metamaterials. *Optics express*, 20(4):3898–917, feb 2012.

[67] S. Mukherjee, A. Spracklen, D. Choudhury, N. Goldman, P. Öhberg, E. Andersson, and R. R. Thomson. Observation of a Localized Flat-Band State in a Photonic Lieb Lattice. *Physical review letters*, 114(24):245504, jun 2015.

[68] R. A. Vicencio, C. Cantillano, L. Morales-Inostroza, B. Real, C. Mejía-Cortés, S. Weimann, A. Szameit, and M. I. Molina. Observation of Localized States in Lieb Photonic Lattices. *Physical review letters*, 114(24):245503, jun 2015.